Monthly Notices of the ROYAL ASTRONOMICAL SOCIETY

MNRAS **532,** 3625–3642 (2024) https://doi.org/10.1093/mnras/stae1032
Advance Access publication 2024 June 25

Deep *JWST*/NIRCam imaging of Supernova 1987A

Mikako Matsuura [1★] M. Boyer,[2] Richard G. Arendt [3,4] J. Larsson [5] C. Fransson,[6] A. Rest,[2,7] A. P. Ravi [8] S. Park,[8] P. Cigan,[9] T. Temim,[10] E. Dwek,[3] M.J. Barlow [11] P. Bouchet,[12,13] G. Clayton [14] R. Chevalier,[15] J. Danziger,[16] J. De Buizer [17] I. De Looze [18] G. De Marchi,[19] O. Fox [2] C. Gall,[20] R. D. Gehrz,[21] H. L. Gomez,[1] R. Indebetouw,[15,22] T. Kangas [23,24] F. Kirchschlager [11,18] R. Kirshner,[25] P. Lundqvist [5] J.M. Marcaide,[26] I. Martí-Vidal [26,27] M. Meixner,[28] D. Milisavljevic,[29,30] S. Orlando [31] M. Otsuka [32] F. Priestley,[1] A.M.S. Richards,[33] F. Schmidt,[11] L. Staveley-Smith [34] Nathan Smith [35] J. Spyromilio,[36] J. Vink [37,38,39] Lifan Wang,[40] D. Watson,[41,42] R. Wesson [1,11] J. C. Wheeler [43] C.E. Woodward,[21] G. Zanardo [33] D. Alp[5] and D. Burrows[44]

Affiliations are listed at the end of the paper

Accepted 2024 April 15. Received 2024 April 15; in original form 2023 September 1

ABSTRACT

JWST/NIRCam obtained high angular resolution (0.05–0.1 arcsec), deep near-infrared 1–5 μm imaging of Supernova (SN) 1987A taken 35 yr after the explosion. In the NIRCam images, we identify: (1) faint H_2 crescents, which are emissions located between the ejecta and the equatorial ring, (2) a bar, which is a substructure of the ejecta, and (3) the bright 3–5 μm continuum emission exterior to the equatorial ring. The emission of the remnant in the NIRCam 1–2.3 μm images is mostly due to line emission, which is mostly emitted in the ejecta and in the hotspots within the equatorial ring. In contrast, the NIRCam 3–5 μm images are dominated by continuum emission. In the ejecta, the continuum is due to dust, obscuring the centre of the ejecta. In contrast, in the ring and exterior to the ring, synchrotron emission contributes a substantial fraction to the continuum. Dust emission contributes to the continuum at outer spots and diffuse emission exterior to the ring, but little within the ring. This shows that dust cooling and destruction time-scales are shorter than the synchrotron cooling time-scale, and the time-scale of hydrogen recombination in the ring is even longer than the synchrotron cooling time-scale. With the advent of high sensitivity and high angular resolution images provided by *JWST*/NIRCam, our observations of SN 1987A demonstrate that NIRCam opens up a window to study particle-acceleration and shock physics in unprecedented details, probed by near-infrared synchrotron emission, building a precise picture of how an SN evolves.

Key words: circumstellar matter – dust, extinction – ISM: supernova remnants – infrared: ISM.

1 INTRODUCTION

The explosion of Supernova (SN) 1987A was detected on 1987 February 23,[1] in a neighbouring galaxy, the Large Magellanic Cloud, at a distance of 49.6 kpc (Pietrzyński et al. 2019). This is the nearest SN explosion detected in 400 yr, since *Kepler*'s SN in 1604 (McCray 1993). Due to its proximity, SN 1987A can be well resolved with modern telescopes, and was observed at almost every wavelength from the γ-ray to the radio (Arnett et al. 1989).

The iconic *Hubble Space Telescope (HST)* optical image of SN 1987A consists of the inner ejecta, the equatorial ring, and the outer rings. These components are also illustrated by our image (Fig. 1),[2] taken by NIRCam (Rieke et al. 2023) on board the *JWST* (Gardner et al. 2023). The equatorial and outer rings are circumstellar material that was ejected from the progenitor (Jakobsen et al. 1991; Crotts, Kunkel & Heathcote 1995). It is not known exactly how these rings were formed, but most likely the process involved a binary system (e.g. McCray 2003). It has been suggested that until about 20 000 yr ago, the progenitor star was a red supergiant (Crotts & Heathcote 1991). The mass-loss wind from the red supergiant was diverted to an equator by a binary system, and this process may eventually have led to the formation of the iconic rings around SN 1987A (Lloyd, O'Brien & Kahn 1995). Morris & Podsiadlowski (2007) further proposed that the merger of a binary companion spun out the rings, and at the same time the merger turned the progenitor into a blue supergiant. However, it still remains unknown when and how the progenitor turned into a blue supergiant, but it could involve dredge-up or binary merger (Saio, Nomoto & Kato 1988; Arnett et al. 1989; Fransson et al. 1989). A few Galactic examples of similar rings are seen around blue supergiants and luminous blue variables (Brandner et al. 1997; Smith 2007; Smith, Bally & Walawender 2007; Smith et al. 2013).

★ E-mail: matsuuram@cardiff.ac.uk

[1] http://www.cbat.eps.harvard.edu/iauc/04300/04316.html

[2] The image is modified from the original image published at https://webbtelescope.org/contents/media/images/2023/136/01H8Q02S452MC9CAF0VSJ3ZTFX

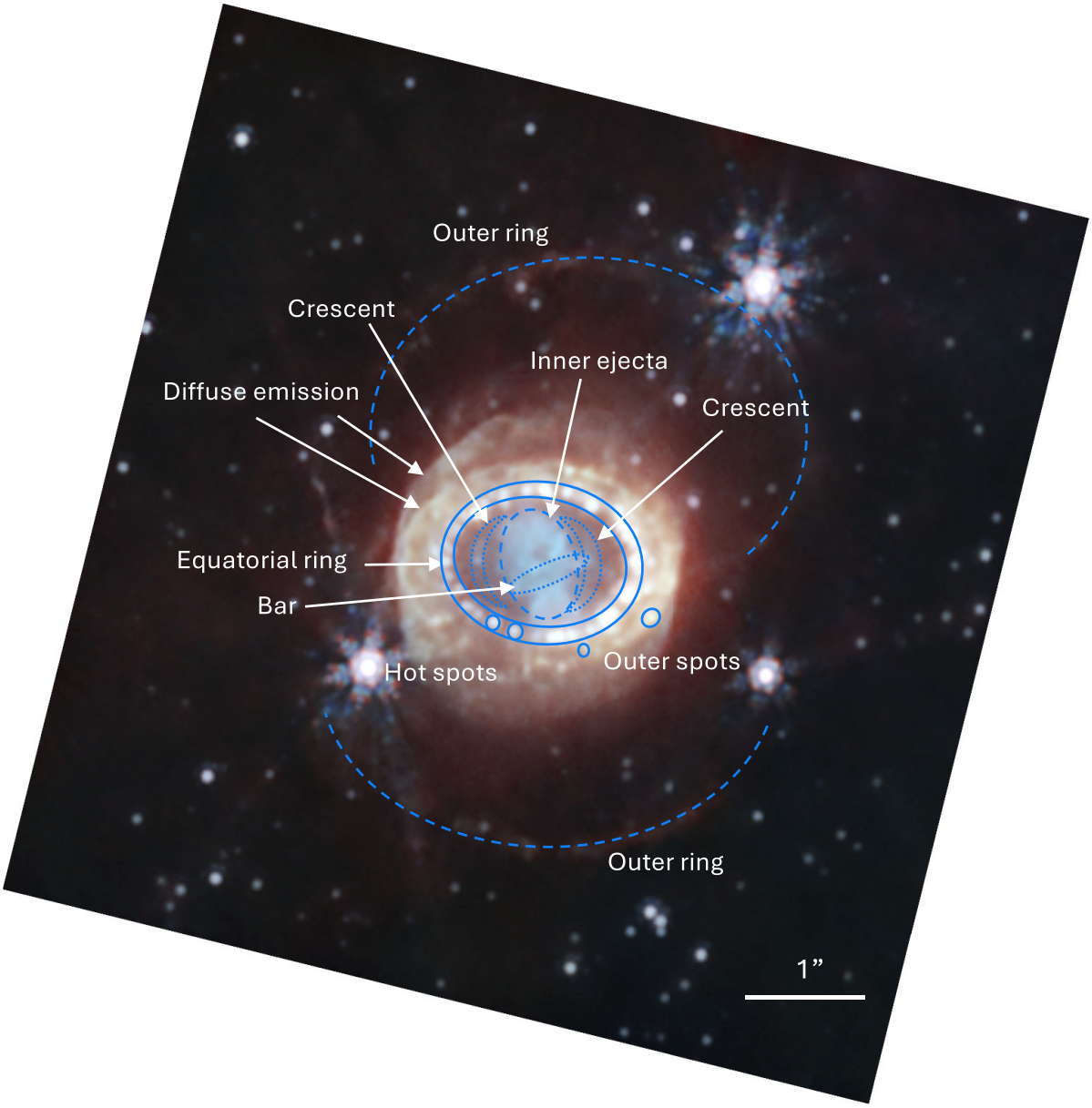

Figure 1. NIRCam five-colour image (blue: *F150W*, cyan: *F164N*, cyan: *F200W*, yellow: *F323N*, orange: *F405N*, and red: *F444W*), capturing the bright equatorial ring, shocked gas beyond the equatorial ring, and the very faint outer rings. The inner ejecta stands out in cyan as it has strong *F164N* emission. Within the inner ejecta, a bar crosses across approximately from the east to west. Two crescents are found in very faint blue/cyan emission between the inner ejecta and the equatorial ring. The hotspots are bright spots in the NIRCam/SW images within the equatorial ring, while the outer spots are found exterior of the equatorial ring. North is towards the top and east is to the left. The original image was created by Alyssa Pagan (STScI), and the image credits belong to NASA, ESA, CSA, Mikako Matsuura (Cardiff University), Richard Arendt (NASA-GSFC, UMBC), Claes Fransson (Stockholm University), and Josefin Larsson (KTH).

The outer ejecta expand with a speed exceeding 10 000 km s^{-1} (Phillips et al. 1988; McCray 1993), triggering shocks within the circumstellar material. Shocks brightened the equatorial ring (labelled in Fig. 1) in about 1995 (Sonneborn et al. 1998; Lawrence et al. 2000), and the brightness increased in X-ray, optical, infrared (IR) and radio until about 2010 (Dwek et al. 2010; Fransson et al. 2015; Frank et al. 2016). Approximately in 2010, the shocks passed the equatorial ring, and material outside of the equatorial ring is now detected as faint outer spots (labelled in Fig. 1) in the optical images (Fransson et al. 2015; Larsson, Fransson & Alp 2019). Around this time, the light curves in different bands started to diverge. The hard X-ray and radio brightness continued to increase (Frank et al. 2016; Cendes et al. 2018), though at a slower rate than before 2003. Meanwhile, the near-infrared (NIR) brightness, as observed using *Spitzer*, peaked around 2010 and started declining thereafter (Arendt et al. 2016, 2020). The cause of diverged light curves at different wavelengths was unknown. The mid-IR emission is known to be from silicate dust in the equatorial ring (Bouchet et al. 2006; Dwek et al. 2010; Arendt et al. 2016; Matsuura et al. 2022). Although it has been suggested to be ‘hot’ (∼500 K) dust (Bouchet et al. 2006;

Table 1. *JWST*/NIRCAM observations of SN 1987A.

Channel	Filter	λ_p	BW	λ_B	λ_R	PSF	$t_{\rm exp}$	$I_{\nu\,\rm BK}$	$\sigma I_{\nu\rm BK}$	Error
Short	*F150W*	1.501	0.318	1.331	1.668	0.05	1347	0.175	0.067	0.134
	*F164N**	1.645	0.02	1.635	1.653	0.056	37 716	0.802	0.112	0.059
	F200W	1.989	0.457	1.755	2.226	0.066	1155	0.235	0.081	0.131
	F212N	2.121	0.027	2.109	2.134	0.072	28 287	0.782	0.084	0.058
Long	*F323N**	3.237	0.038	3.217	3.255	0.108	28 287	−0.015	0.007	0.05
	F356W	3.568	0.781	3.14	3.98	0.116	1347	−0.418	0.004	0.067
	*F405N**	4.052	0.045	4.028	4.074	0.136	37 716	0.485	0.071	0.034
	F444W	4.408	1.029	3.88	4.986	0.145	1155	−0.02	0.014	0.066

λ_p: pivot wavelength in μm (Tokunaga & Vacca 2005). BW: bandwidth in μm. λ_B and λ_R: the half-power wavelengths in μm of a passband at blue and red wavelengths, at which the transmission falls to 50 per cent of its peak value.
PSF: FWHM of the empirical PSF. $t_{\rm exp}$: exposure time on source in sec. $I_{\nu,\,\rm BK}$ and $\sigma I_{\nu\rm BK}$: mean and 1σ of 'blank sky' level in a nearby field (MJy sterad^{-1}). Error: mean error level estimated from the error map in a nearby field but off from SN 1987A. This error combines Poisson noise and read noise (MJy sterad^{-1}). **F164N*, and *F323N,* and *F405N* filters are used together with the wide-band filters *F150W*, *F322W2*, and *F444W*, respectively.

Dwek et al. 2010), the emitting region and the source of the NIR 3–4 μm flux was not well established, because no instrument had the resolution and sensitivity to clearly spatially resolve SN 1987A at 3–4 μm before *JWST*. Modelling the total flux of NIR to mid-IR spectra from *JWST*/NIRSpec and Mid-Infrared Instrument (MIRI) shows that the combination of dust, synchrotron, and atomic emission contributes to overall emission at this wavelengths (Jones et al. 2023; Larsson et al. 2023). NIRCam imaging provides the highest angular resolution and best sensitivity available with *JWST*, and can pinpoint the emitting regions of different components of dust, synchrotron, and atomic lines (Arendt et al. 2023). This will allow us to understand precisely the physics of dust, synchrotron, and atomic line emission in shocked and post-shocked regions in SN 1987A, enabling us to witness the real-time physics of an evolving SN.

2 *JWST*/NIRCAM OBSERVATIONS OF SN 1987A

We obtained deep images of SN 1987A, using NIRCam on *JWST* under general observer program 1726. The data were acquired on 2022 September 1 and 2, days 12 974 and 12 975 after the SN explosion was first detected. NIRCam has a short wavelength channel (0.6–2.3 μm, hereafter SW) and a long-wavelength channel (2.4–5.0 μm, hereafter LW). Eight filters were used: four in the SW channel, and four in the LW channel. The properties of the filters are summarized in Table 1.

We chose to use the subarray of NIRCam detectors rather than using the full array, because this observing mode saves total observing time and avoids total saturation by nearby field stars. SN 1987A measures approximately 8 arcmin across its outer rings, and the whole system was completely covered by the 320 × 320 pixel subarray of the detector by the SUB320 mode of the Module B camera. In the SW channel, the total area covered is approximately 25 arcsec × 25 arcsec, with a ∼5 arcsec gap between the subarrays of the four detectors. In the LW channel, the field of view is 20.45 arcmin × 20.50 arcmin using a single subarray (with larger pixels). Fig. 2 demonstrates the coverage of SUB320 images of the LW channel. The NIRCam pixel scales are 0.0317 arcmin in the SW channel and 0.0647 arcmin in the LW channel. The full width at half-maxima (FWHM) of the point spread functions (PSF) are 0.066 arcmin at *F200W* and 0.16 arcmin at *F356W*.[3] The RAPID

[3]https://jwst-docs.stsci.edu/jwst-near-infrared-camera/nircam-performance/nircam-point-spread-functions

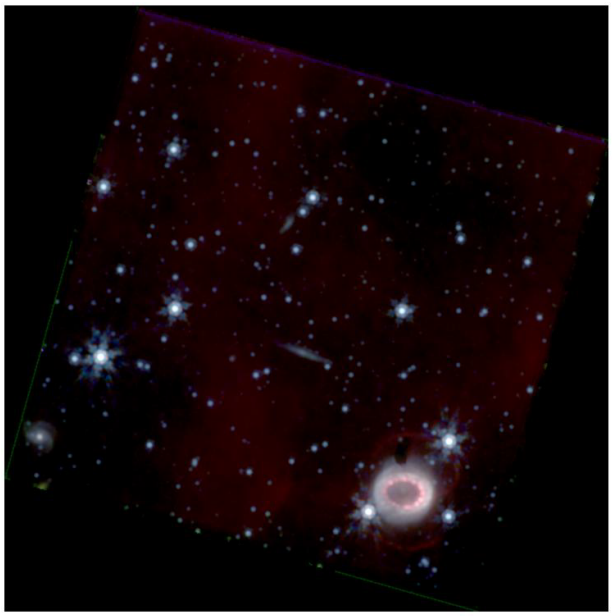

Figure 2. NIRCam long wavelength channel images, covering the entire field of view around SN 1987A. North is top, east is to the left, and the area covers 25.4 arcmin × 25.2 arcmin. The colour allocations are – blue: *F323N*, green: *F356W*, red: *F405N*, and brown: *F444W*.

reading mode was chosen for wide-band filters, while MEDIUM 8 was used for longer exposures with the narrow-band filters. The total exposure times on source are summarized in Table 1, ranging from 1155 to 37716 s per filter band.

The NIRCam sensitivities were approximately 30 per cent better than the pre-flight prediction (Rigby et al. 2023). As a consequence, we achieved 0.004–0.11 MJy sr^{-1} at 1σ noise levels, measured in a blank sky area (Table 1), which constitutes very deep imaging of SN 1987A. Fig. 2 shows that this deep image can detect Brα emission in the ambient interstellar medium, evident as the patchy background emission in *F405N* filter (red).

2.1 Data reduction

The NIRCam data were reduced using the JWST Calibration Pipeline (Bushouse et al. 2023) software version 2022_3. The calibration

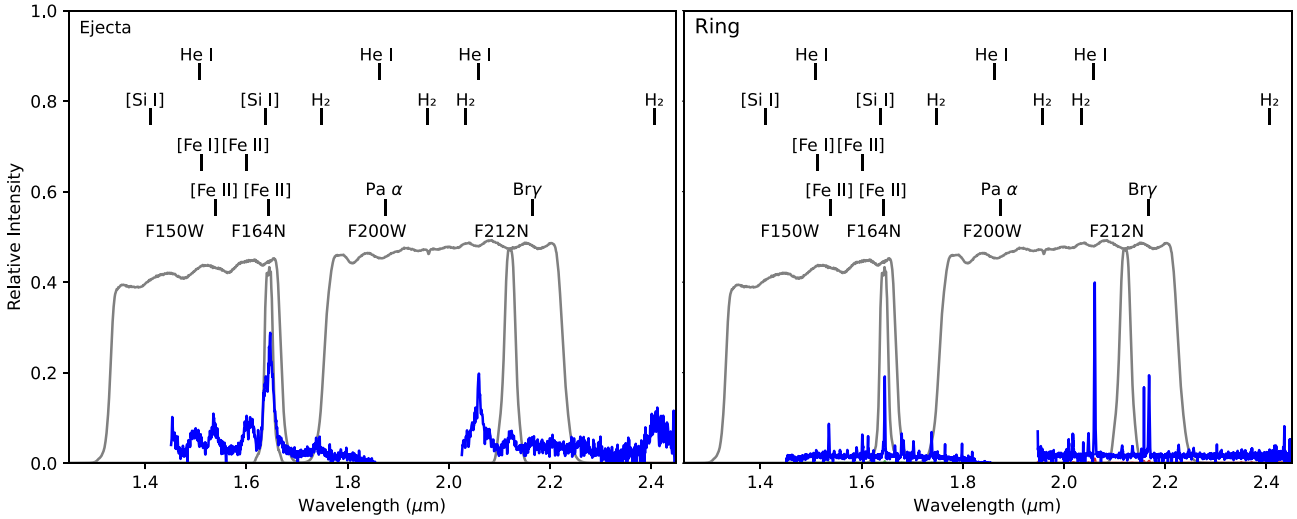

Figure 3. The filter transmission curves of the NIRcam short wavelength channel (grey lines with filter names above). SINFONI spectra of the ejecta (left) and ring (right) in *H* and *K* bands (Larsson et al. 2016) are also plotted in blue lines, with line identifications labelled.

software version number was 1.8.5 with CRDS version 11.16.16 and CRDS context jwst_1023.pma. 1/*f* noise was removed.

Field stars were used to align NIRCam images with different jitter positions, as well as for absolute astrometry. First, an *HST* ACS *(Advanced Camera for Surveys) F656W* image observed in 2003 (Tziamtzis et al. 2011) was aligned with 23 *Gaia* stars (Gaia Collaboration 2018) in the field of view, and the astrometry of the *HST* image was corrected. The *HST F656W* image was fed into NIRCam Aperture Photometry PYTHON code,[4] which is part of JDAT_NOTEBOOKS to create a point source catalogue within the *HST* field, with coordinates measured from the *HST* image. This catalogue was cross-matched against point sources in all NIRCam images; about 50–100 point sources were detected in common between NIRCam images and the *HST* image. The coordinates of these sources were used to correct image distortion, jittered image frames, and to perform astrometry. A colour composite of the NIRCam LW images covering the entire field of view around SN 1987A is shown in Fig. 2.

2.1.1 *Image convolutions*

In order to derive colours from two images, the angular resolutions must be matched. For this process, the images were convolved with PSFs. Simulated PSFs were calculated using WebbPSF (Perrin et al. 2014). The convolution was processed, using the PYTHON code PSF MATCHING (Gordon et al. 2008; Aniano et al. 2011). This module creates a common resolution kernel from the simulated PSFs for each convolution operation between higher- and lower-resolution filters. Window functions in signal processing are generally used to taper out the high-frequency noise generated during Fourier transformations within convolution algorithms (Harris 1978). Thus, we implemented a Cosine Bell (also called a Hanning) window for convolutions between short- and long-wavelength channel filters. On the other hand, a split Cosine Bell window was used for convolutions among filters within the short- and long-wavelength channels.

2.2 Line emission within filter bands

In order to assess the important line and continuum contributions to filter bandpasses, we used the spectra from European Southern Observatory's (ESO) SINFONI (Spectrograph for INtegral Field Observations in the Near Infrared) (Larsson et al. 2016) and *JWST*/NIRSpec (Larsson et al. 2023).

Fig. 3 compares the *H*- and *K*-band spectra of SN 1987A with the NIRCam filter transmission curves.[5] These are pre-flight transmission curves and include instrumental throughput. The figure also includes SINFONI (Eisenhauer, Abuter & Bickert 2003) spectra of the SN 1987A equatorial ring and the ejecta in the *H* and *K* bands, that were obtained in 2014 October and December (days 10 090–10 152 since the explosion; Larsson et al. 2016). The line identifications are taken from Kjær et al. (2007) and Larsson et al. (2016, 2023). H_2 line wavelengths are from Roueff et al. (2019).

The broad-band filters, in particular those in the SW channel, contain some strong lines, as detected in the *JWST*/NIRSpec observations (Larsson et al. 2023). These strong lines are listed in Table 2. Between the ejecta and the equatorial ring, different lines contribute to filter bandpasses, so that they are listed separately in the table.

The *F150W* band has contributions from [Fe I], [Fe II], and [Si I] lines in the ejecta and [Fe II] lines in the equatorial ring. The *F200W* filter has contributions from Paα, He I, and $H_2 v = 1$–0 S(3) and S(2) lines in the ejecta, while the ring is dominated by atomic lines such as H I (both Paα and Brγ), and He I lines.

The *F164N* filter has contributions from both the [Fe II] and [Si I] lines in the ejecta. With respect to the 1.64355 μm (vacuum wavelength) [Fe II] $a^4D_{7/2}$–$a^4F_{9/2}$ line, the half-power bandwidth of the *F164N* filter covers velocities from -1855 to $+1426\,\mathrm{km\,s^{-1}}$, where the systematic velocity of SN 1987A of $+\ 287\,\mathrm{km\,s^{-1}}$ (Meaburn, Bryce & Holloway 1995) is accounted for. Although a majority of the line intensity from the [Fe II] falls within the *F164N* filter band, the line width extends beyond $\pm 2000\ \mathrm{km\,s^{-1}}$ (Larsson et al. 2016), so the *F164N* filter band misses the fast components. The [Si I] 1.64545 μm line also falls in the

[4] https://spacetelescope.github.io/jdat_notebooks/notebooks/aperture_photometry/NIRCam_Aperture_Photometry_Example.html

[5] https://jwst-docs.stsci.edu/jwst-near-infrared-camera/nircam-instrumentation/nircam-filters

Table 2. The strong lines falling into the NIRCam filter bands (with their vacuum wavelength in μm). Lines are listed separately for the ejecta and the equatorial ring, and are taken from Larsson et al. (2023).

Channel	Filter	Ejecta	Ring	Note
Short	*F150W*	[Fe I] 1.444; [Si I] 1.607; [Fe II] + [Si I] 1.64 blend	[Fe II] 1.534; [Fe II] 1.600; [Fe II] 1.644	
	F164	[Fe II] + [Si I] 1.64 blend	[Fe II] 1.644	
	F200W	H I 1.875 (Paα); He I 2.059; H_2 2.122	H I 1.875 (Paα); He I 2.059; H I 2.166 (Brγ)	
	F212	H_2 2.122 $v = 1{-}0$ S(1)	He I 2.114; [Fe II] 2.135	
Long	*F323N*	($H_2 v = 1{-}0$ O(5))		Continuum
	F356W	H_2 3.846; Unidentified $\sim$3.88μm	H I 3.297; H I 3.744	Lines weak relative to continuum
	F405N	H I 4.052 (Brα)	H I 4.052 (Brα)	
	F444W	H I 4.052 (Brα); H I 4.654; H_2 4.695	H I 4.052 (Brα); H I 4.654	

F164N bandpass, and the filter width corresponds to -2203 to 1082 km s^{-1} in the rest frame. In the ejecta as a whole, the SINFONI and NIRSpec spectra show that the line intensity ratio of [Fe II] to [Si I] is approximately 1/3 to 1/2 (Jerkstrand, Fransson & Kozma 2011; Larsson et al. 2023). The ratio of the contribution of the two lines to the intensity in the *F164N* band might be slightly different at different locations. In the ring, the 1.644 μm [Fe II] line dominates the line intensity, and little contribution from [Si I] line is present. Similarly, the *F212N* filter covers the H_2 $v = 1{-}0$ S(1) line from -1432 to 2100 km s^{-1} and the *F405* filter covers Brα from -1319 to 2083 km s^{-1}. The majority of the intensities of these lines are within the filter bands, but the broader (but fainter) components are not covered by these narrow-band filters.

The fluxes of the LW channel have more contribution from the continuum. The NIRSpec spectra of the ejecta and the equatorial ring show that the continuum rises with wavelength both in the equatorial ring and in the ejecta (Larsson et al. 2023).

Although the *F323N* filter was designed to detect the 3.234 μm $H_2 v = 1{-}0$ O(5) line (Black & Dishoeck 1987), the image of SN 1987A in this filter is similar to those made using the broad-band filters of the LW channel, in particular *F356W*. We conclude that the *F323N* flux is dominated by the continuum rather than the H_2 line in all features, except for faint crescent-shaped structures observed between the ejecta and the equatorial ring. This will be explored further in Matsuura et al. (in preparation).

2.2.1 *Auxiliary data: ALMA*

ALMA observed SN 1987A with two tunings, 301.75–305.57 GHz in kinematic local standard of rest (993.51–981.09 μm) and 313.73–317.52 GHz (955.57–944.17 μm), on 2021 November 2 as part of the Project 2021.1.00707.S. The total integration time was 10 813 s. The synthesized beam was 0.081 arcsec $\times$ 0.061 arcsec with a position angle of 33.7° for the major axis. The shortest baselines allowed for a maximum recoverable scale of 0.993 arcsec. This implies that the diffuse emission, which extends more than 1 arcsec, is likely to be over-resolved, resulting in some flux loss.

3 RESULTS AND DISCUSSIONS

SN 1987A contains three major components which we describe separately, namely, the inner ejecta (Section 3.1), the equatorial ring and associated diffuse emission (Sections 3.2 and 3.3), and the outer rings (Section 3.4). Fig. 1 highlights these features using the NIRCam images.

The main findings of the NIRCam images are (1) the substructure of the ejecta, namely, the bar (Section 3.1.1), (2) crescents, faint emission between the ejecta and the equatorial ring, and (3) the first identifications of the NIR synchrotron emission from the hotspots, which are bright spots composing of the equatorial ring, the outer spots and diffuse emission, which are exterior to the equatorial ring (Sections 3.2 and 3.3). The analysis of crescents will be reported in a separate paper.

3.1 Ejecta

The ejecta are detected in all four filter band images in the SW channel (Fig. 4). The keyhole or hourglass shape of the ejecta extends from the north to the south. The ejecta contain a dip or 'hole' near the centre with a slight offset to the north. This 'hole' is not a hole in the gas, but probably due to the heavy extinction (self-absorption) by recently formed SN ejecta dust (Matsuura et al. 2011; Indebetouw et al. 2014; Cigan et al. 2019). At the waist of the ejecta, a small bar is seen from the east to the west in blue colour in Fig. 1 and *F150W* and *F164N* images (Fig. 4). The southern part of the ejecta breaks into two branches near the equatorial ring.

On the other hand, the LW images do not show a clear keyhole shape in the ejecta (Fig. 5). Instead, there are two faint blobs in the north and the south in the *F323N* and *F356W* images. In fact, the northern blob in the *F323N* and *F356W* images corresponds to the hole in the SW channel images. In the middle of the two blobs, a 'gap' spreads from the east to the west. The exception is the *F444W* image, which shows a hint of the keyhole shape and the bar, similar to that seen in the SW images.

The ratio of *F444W*/*F356W* in Fig. 6 (right bottom) indicates an excess in *F444W* in the bar. This suggests that the dust self-absorption towards the bar is still strong at *F356W*, while the dust self-absorption is less in *F444W*.

While the SW bands have emission line contributions, the ejecta emission in the LW bands is dominated by continuum emission (see Section 3.3 and Fig. 11; also Larsson et al. 2023). The NIRCam spectral energy distribution (SED) decomposition analysis shows that in the LW bands the ejecta fluxes are indeed dominated by the continuum (Arendt et al. 2023). The source of the continuum is presumably from cold SN ejecta dust (Matsuura et al. 2011, 2015; Indebetouw et al. 2014). The ALMA (Atacama Large Millimeter/submillimeter Array) continuum images at 450 and 870 μm show more dust towards the centre of the system (Cigan et al. 2019). This causes dust self-absorption around the waist of the ejecta at NIR wavelengths, which is seen as a dip at the centre of the ejecta in NIRCam images. As dust extinction is higher at the shorter wavelength of the NIR, the SW images of this area trace mainly the foreground of the heavily obscured dusty regions in the ejecta.

The dust emission extends across the ejecta (Cigan et al. 2019), but is fainter towards the north and south edges of the ejecta, causing less extinction at NIR wavelengths. These regions are also heated by the

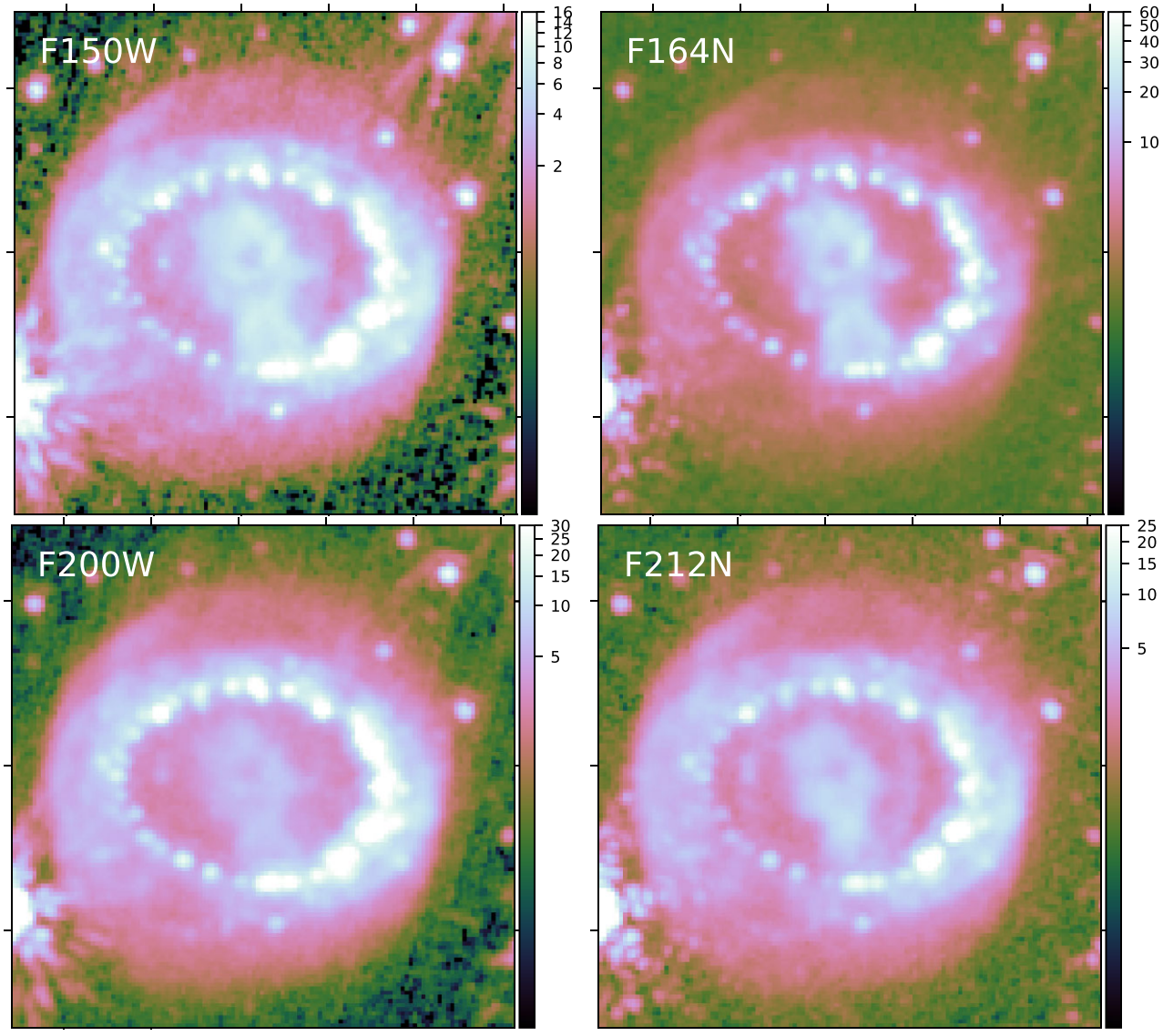

Figure 4. Short-wavelength channel images of the equatorial ring and the faint extended emission beyond the ring and ejecta. Within the ejecta, a bar, extending from the east to the west is found. The equatorial ring consists of more than 20 hotspots, while over 10 outer spots exterior to the equatorial ring are detected. Faint diffuse emission extends far beyond the outer hotspots. The coverage of the images is 3 arcmin × 3 arcmin, with the north at the top, and the colour stretch is in the unit of MJy sr^{-1}.

UV radiation from the equatorial ring, hence, the NIR emission is detected as blobs in the LW images. The total flux of the ejecta is about 12 μJy at *F356W*. Extrapolating the cold (∼20 K) dust emission from the millimetre wavelengths to the NIR would result in less than 1 μJy at *F356W*. Ejecta dust must be heated to temperatures higher than 20 K in the blobs to emit 12 μJy in this band. The obscuration of the hole is seen because cold dust in the centre absorbs the emission from the dust in the far end of the warmer ejecta.

3.1.1 Bar

The bar is a small structure, sticking out to the east and to the west at the waist of the ejecta (Figs 1 and 4). The east component of the bar is slightly tilted to the southeast. The west side of the bar has been detected by *HST* Hα imaging before (e.g. Larsson et al. 2013), but in the optical images, the east side of the bar was not detected clearly. This indicates dust extinction in the line of sight on the east side of the bar.

The apparent structure of the bar slightly differs from one wavelength to another (Fig. 4). In the *F164N* image, the bar looks like a triangular shape, separated from the main body of the ejecta. The bar is also found in the *F150W* and *F200W* images, but less distinct than in *F164N*. In the *F212N* image, there is only a faint trace of the bar structure. This shows that the emission causing the bar is mainly from the atomic lines such as [Fe II] + [Si I] (*F150W* and *F164N*) and probably also [Fe I] at 1.44 μm in *F150W*, or H I and He I (*F200W*), but not H_2 (*F212N*).

At the location of the bar, there is a dip in surface brightness in *F323N* and *F356W* (Fig. 5). Fig. 7 shows the *F356W* image in colour, with contours of the *F164N* image. The bar in the *F164N* image corresponds to the location of the low surface brightness region in the *F356W* image. The waist of this bar also contains some emission of the dust in the ALMA 315 GHz image (Fig. 8). This region probably contains a large mass of dust, so that it absorbs and scatters near-IR light. If there is substantial IR extinction, the [Fe II], [Si I], H I, and

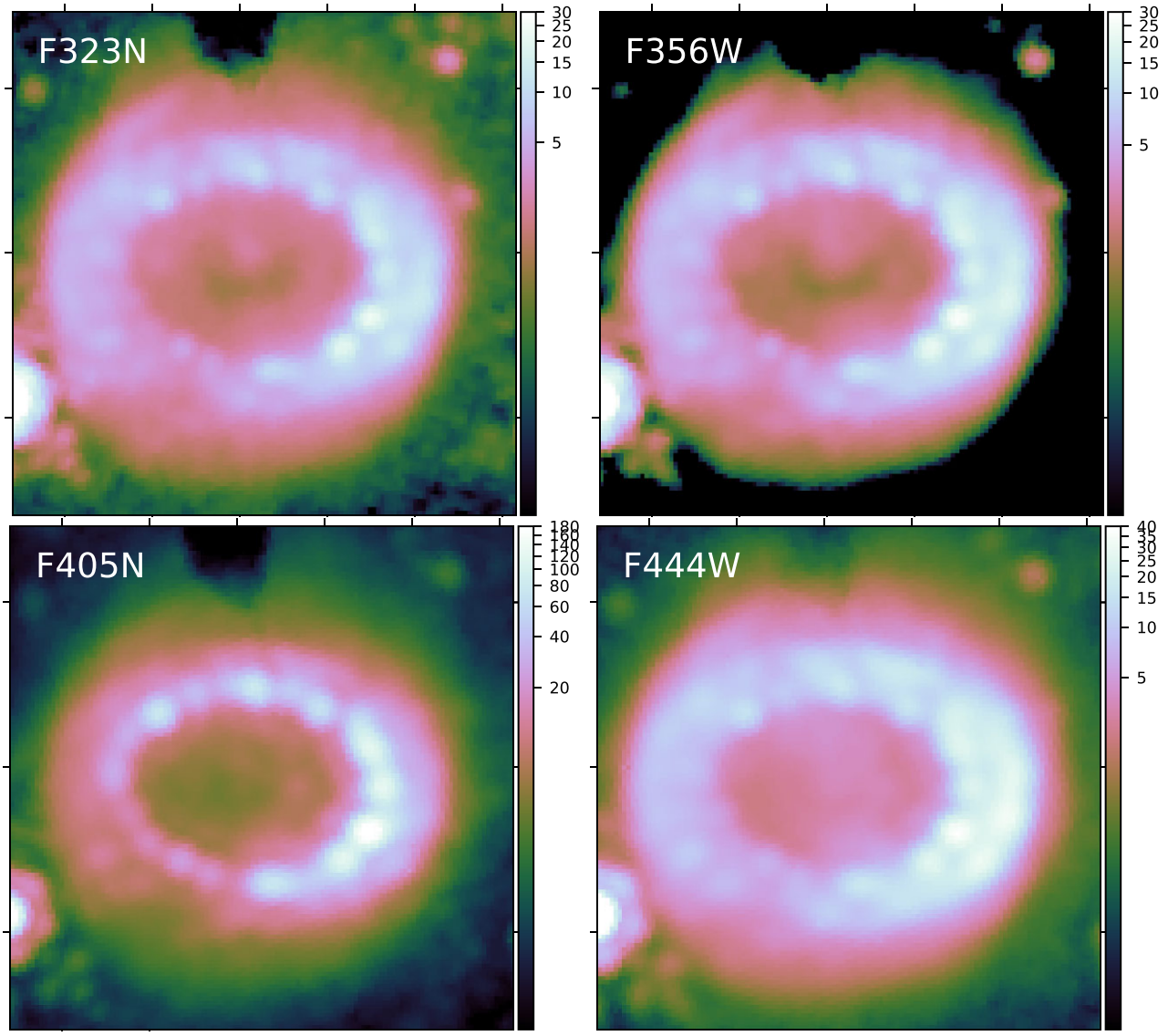

Figure 5. NIRCam LW channel images. The outer spots exterior to the equatorial ring are as bright as the hotspots within the ring in the LW images, apart from *F405N*. The ejecta emission in the LW images is dominated by continuum, mostly due to dust. The dip in the centre of *F343N*, *F356W*, and *F405N* is caused by dust self-absorption. Only two blobs are detected in these images. The *F405N* image traces both the dust continuum and Brα in the ejecta. The coverage of the images is 3 arcmin × 3 arcmin, with the north at the top, and the colour stretch is in the unit of MJy sr^{-1}.

He I emission must come from the surface of the bar structure on the near side to us, and therefore does not reflect the whole structure of the bar.

3.1.2 *[Si I] and [Fe II] emission*

In general, the 1.64 μm [Fe II] line is often used as a tracer of shocks. In SN remnants, there is the complication of blending of two lines ([Si I] and [Fe II]) in the *F164N* filter. These two atomic stages have quite different ionization potentials. Fe^+ has an ionization potential of 16.2 eV (Mouri, Kawara & Taniguchi 2000). The ionization energy of Si^0 is only 8.2 eV.

The top left panel of Fig. 6 shows the ratio of the *F164N* image to the *F150W* image ($I_{\nu\,\mathrm{F164N}}/I_{\nu\,\mathrm{F150W}}$). The interpretation of this image requires some caution, because the *F150W* image, which is typically expected to be a continuum, actually contains atomic lines, such as [Fe I]. Nevertheless, the ratio image combined with the *F164N* image should show characteristics of the [Si I] and [Fe II] emitting regions, as the *F164N* intensity is typically three times brighter than the *F150W* intensity in the ejecta.

The $I_{\nu\,\mathrm{F164N}}/I_{\nu\,\mathrm{F150W}}$ ratio in Fig. 6 shows two peaks, one at the north–northeast and the other at the northwest edges of the ejecta. The primary peak at the northwest ejecta is found in the original *F164N* image, so that this is due to an excess of [Si I] and [Fe II] line intensities, and not due to the dip in the [Fe I] line intensity in *F150W*.

While the 1.64 μm [Fe II] line is often used as a tracer of shocks in supernova remnants (SNRs) or active galactic nuclei, this line in SN 1987A might not be solely due to shock excitation. The excitation mechanisms of lines might be different in the outer and the inner parts of the 'inner ejecta'. (Note that historically, 'outer ejecta' refers to the ejecta with high velocity but low density, extending beyond the keyhole, and some part of this has passed the equatorial ring

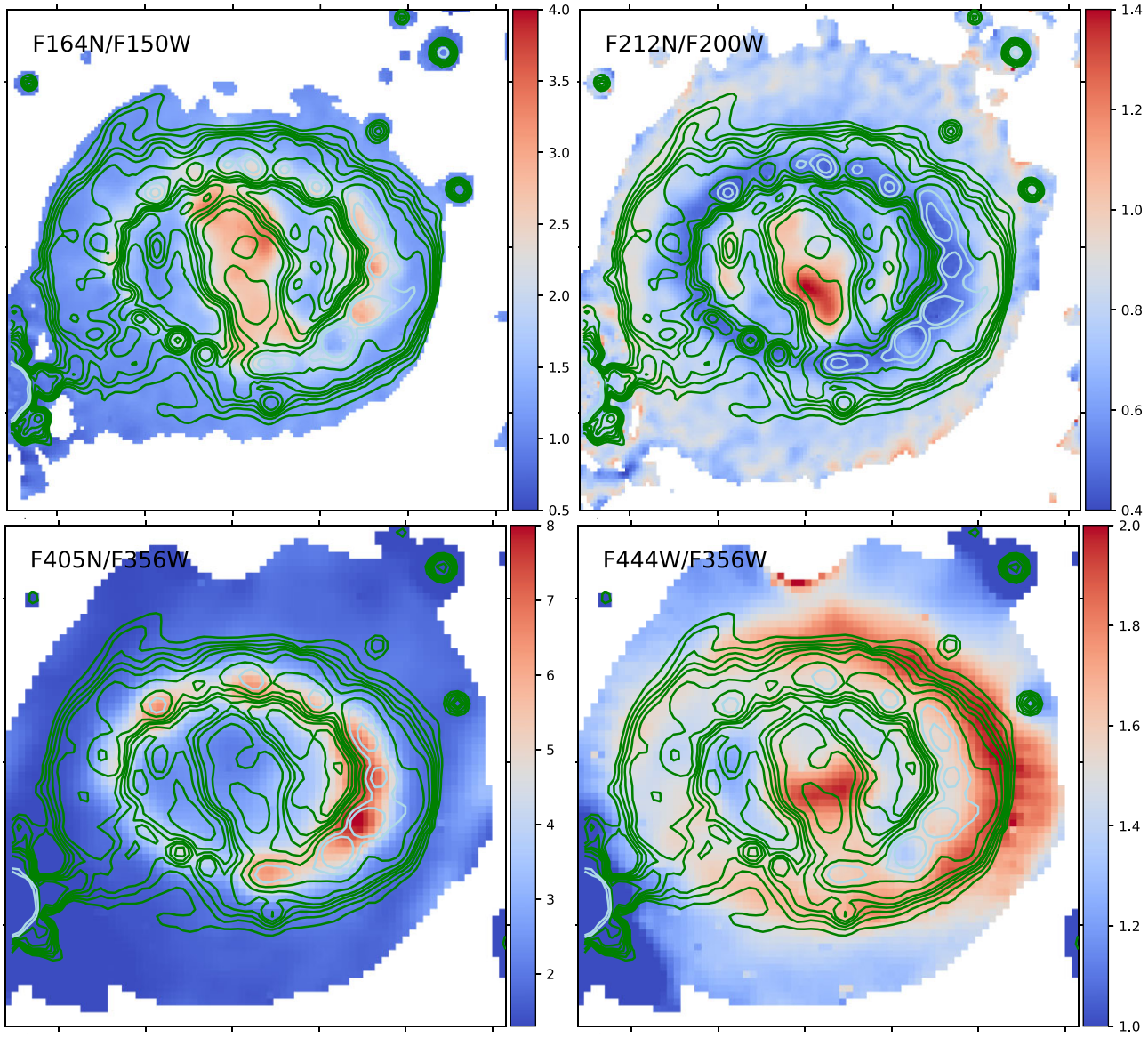

Figure 6. The colours show the intensity ratios of two filter bands. The line contours are plotted to guide the eye; these represent the *F212N* image, smoothed to the angular resolutions of the filter bands used to compute the intensity ratios.

and has been interacting with the ring and its exterior material.) The prominent [Fe II] line at 1.644 μm is due to the $a^4F_{9/2}$–$a^4D_{7/2}$ transition (Mouri et al. 2000). The critical density for collisional de-excitation is $n_{\rm crit} \sim 10^5\,{\rm cm}^{-3}$ at the electron temperature of $T_{\rm e} = 10^4$ K (Shull & Steenberg 1982; Greenhouse et al. 1991). At lower kinetic temperature and lower density, the excitation of the [Fe II] 1.644 μm line is mainly by UV fluorescence and non-thermal excitation and ionization, followed by radiative de-excitation to the upper $a^4F_{9/2}$ level of the 1.644 μm line (Jerkstrand et al. 2011). Thermal collisional excitation is not important in the inner region: it has a very low temperature, only <200 K even at 8 yr after the explosion (Jerkstrand et al. 2011), compared to the excitation temperature of the $a^4F_{9/2}$ level of 11 445 K.

However, thermal collisional excitation may be important for the [Fe II] line in the region close to the ring, where the X-ray photoionization and heating (Fransson et al. 2013) may result in a temperature >2000 K, enough to excite this line. The secondary peak of the emission at the north–northeast of the ejecta close to the equatorial ring (the top left panel of Fig. 6) probably traces the interaction of the ejecta with the equatorial ring at that location (Larsson et al. 2023).

Integrated across the entire ejecta, the [Si I] line is predicted to contribute more to the *F164N* intensity than the [Fe II] line (Larsson et al. 2023). At the primary peak, instead of [Fe II], the [Si I] line might contribute more to the intensity, and its excitation could be due to recombination at temperatures below 200 K (Raymond et al. 2018; Larsson et al. 2023).

3.1.3 *H_2 emission*

The *F212N* image in Fig. 4 and the $I_{\nu\,\rm F212N}/I_{\nu\,\rm F200W}$ ratio in Fig. 6 show the H_2 emitting region in the ejecta. The overall shape of the H_2 emitting region within the ejecta is similar to those of

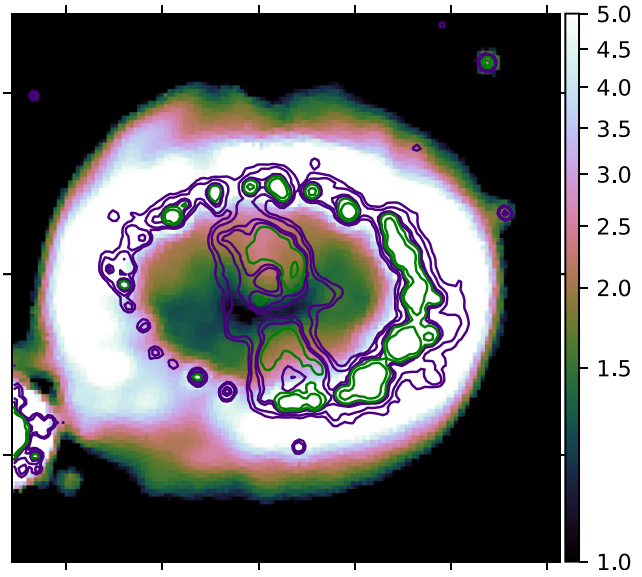

Figure 7. *F356W* image in colour contours in the unit of MJy sr^{-1}, with *F164N* represented by line contours. It looks like that the bar emission in *F164N* is a dip in intensity in the *F356W* image.

the Hα (*F625W*; Larsson et al. 2019) and [Fe II] emitting regions (Fig. 4), but the H_2 peak is located in the south, corresponding to the locations where the Hα and [Fe II] emissions are fainter. The H_2 strength has almost an anticorrelation with the [Fe II] strength: the peak of [Fe II] is in the northwest, and that side of the ejecta has weaker H_2 emission. The anticorrelation can also be found in Hα and H_2 (Larsson et al. 2019). This could be the effect of the strength of the X-ray and 912–1100 Å UV illumination from the equatorial ring onto particular locations within the ejecta. On the west side of the equatorial ring and just outside the ring, there are ongoing strong shocks, while on the southeast side, only weak emission is found from the equatorial ring (Section 3.2; also Frank et al. 2016). The X-ray radiation from the southeast of the ring imprinting onto the southeast part of the ejecta is also weaker, hence, there is more molecular gas found in the southeast than in the rest of the ejecta.

3.1.4 Brα emission

The bottom left image of Fig. 5 is the Brα-dominated *F405N* image, and the $I_{\nu\,\mathrm{F405N}}/I_{\nu\,\mathrm{F356W}}$ ratio in Fig. 6 shows the Brα emitting region in the ejecta. The distinct key-hole shape of the ejecta, found in Fig. 4 and the *HST* Hα image (Larsson et al. 2019), is not obvious in Brα. This is an illusion of the colour stretch used in Fig. 5, and there is a slight dip in the brightness. As seen in Fig. 5, Brα is very faint in the ejecta, compared with the equatorial ring. Nevertheless, the peak of the Brα emission on the west side of the ejecta is part of the bar. Very faint Brα emission from the north of the ejecta is also identified as a blob. It is not clear whether the additional very faint blob on the east side of the ejecta is also due to the bar, with a possible additional contribution from the outer ring.

In the LW channel images, the *F405N* image is distinctly different from the rest of the images (Fig. 5). In the *F323N* and *F356W* images, there are two separate blobs, one in the north and the other in the south of the ejecta. In the *F405N* image, the north blob is detected, but the south blob is missing. It seems that the Brα emission from just inside the equatorial ring is stronger than the Brα emission from the south blob, burying the emission from the south blob.

3.2 The equatorial ring and its exterior

The NIRCam images of SN 1987A captured detailed structures found within and exterior to the equatorial ring (Fig. 1). The equatorial ring is composed of at least 22 hotspots along its circumference. Hotspots are bright parts within the equatorial ring in UV and optical, and in the past, associated with the forward shocks colliding into dense clumps (Sonneborn et al. 1998). They have the highest density within the circumstellar material. These hotspots within the equatorial ring are the brightest structures within the SN 1987A system in the SW images (Fig. 4).

Exterior to the equatorial ring, there are rings of faint diffuse emission. The outer diffuse emission is composed of at least three ellipses, possibly four, though these numbers and shapes are subjective (Fig. 9). Three separate arcs are clearly seen in the northeast part within the diffuse emission (Fig. 4). It is unclear whether ellipses 2 and 4 are actually a single ellipse or two separate ellipses that are offset in the north and south directions. The diffuse emission is expected to be due to the reverse shock (Larsson et al. 2023). *JWST*/NIRSpec observations of the He I 1.083 μm line were used to determine the 3D morphology of the line, which revealed a bipolar shape with bubble-like structures extending outwards on both sides of the equatorial ring (Orlando et al. 2020; Larsson et al. 2023). Projection and limb brightening of the shock surface may create several elliptical structures in the images.

While the faster ($>$ 10 000 km s^{-1}) but low-density outer ejecta expands continuously since the SN explosion (Larsson et al. 2016; Kangas et al. 2022), it interacts with the circumstellar envelope. Until about 2014, the locations of the main interactions of the outer SN ejecta with the circumstellar material were within the equatorial ring (France et al. 2015). This interaction is now most actively occurring at the equatorial ring on the north and west sides and the exterior to the equatorial ring. The interaction causes emission, which contains continuum emission (a combination of synchrotron and dust, discussed in the next section) and line emission, and appears as diffuse emission outside of the equatorial ring. Diffuse emission is detected by *HST* (Larsson et al. 2019) but it is clearer in *JWST* NIRCam images, because of the brighter contribution of synchrotron emission in the NIR than in the Hα emission observed with *HST*.

In these diffuse rings, we found spots, which we refer to as 'outer spots' to distinguish them from the hotspots within the equatorial ring (Larsson et al. 2019). These outer spots and hotspots are spatially unresolved at the NIRCam angular resolutions (FWHM of $<$0.05 arcsec; Table 1). Having outer spots within the diffuse ring suggests that the mass-loss material from the red supergiant may not have been smooth, but had contained many clumps within. As the thin but faster SN ejecta expands and collides with the circumstellar material, the gas in these clumps is now ionized and shocked, and forms as 'outer spots'.

Fig. 5 shows that the outer spots are as bright as the hotspots, or even brighter on the east side in the LW images, except for in the *F405N* image. These images are in contrast to the SW images, which show brighter hotspots than the outer spots. The outer spots in the LW images appear to form an outer portion of the equatorial ring, extending all around it (Arendt et al. 2023). In general, both the hotspots and the outer spots are brighter on the western side than on the eastern side.

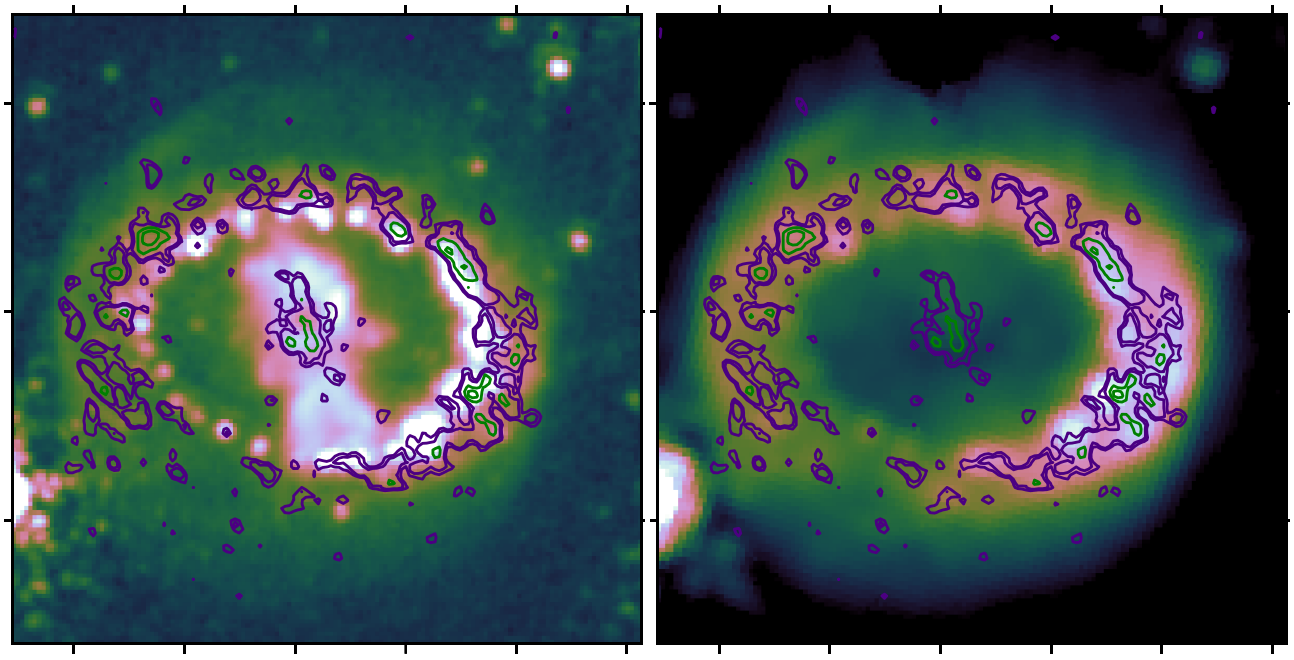

Figure 8. *F164N* image (left) and *F356W* image (right) with ALMA 315 GHz continuum emission shown as line contours. The ALMA continuum image contains synchrotron radiation in the ring and dust thermal emission in the ejecta. The hotspots and the outer spots detected in the *F356W* image generally have corresponding spots in ALMA 315 GHz synchrotron emission.

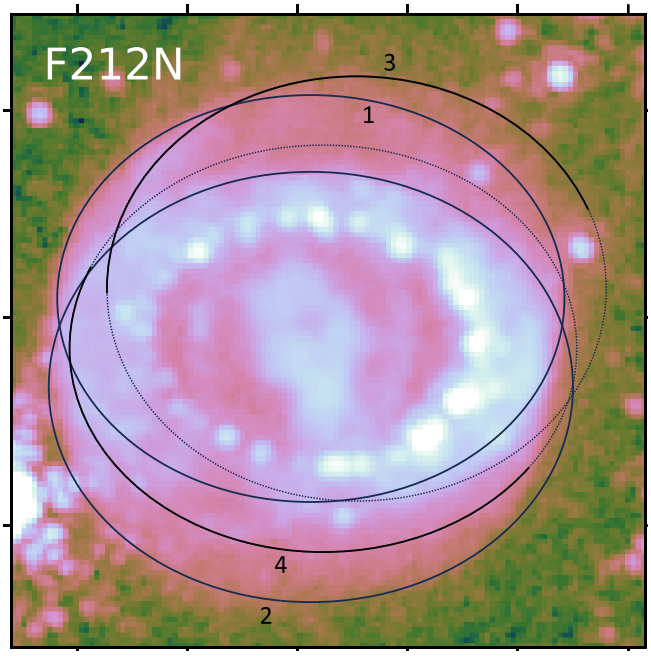

Figure 9. Illustrating the three or four faint ellipses within the diffuse emission. The ellipses 1 and 2 have well-defined edges, while ellipses 3 and 4 have partial ellipses, and their full structures are not clear. Ellipse 4, tracing on the south part of the diffuse emission, might be tracing a few outer spots, rather than a full ellipse, so that the total number of ellipses could be three or four.

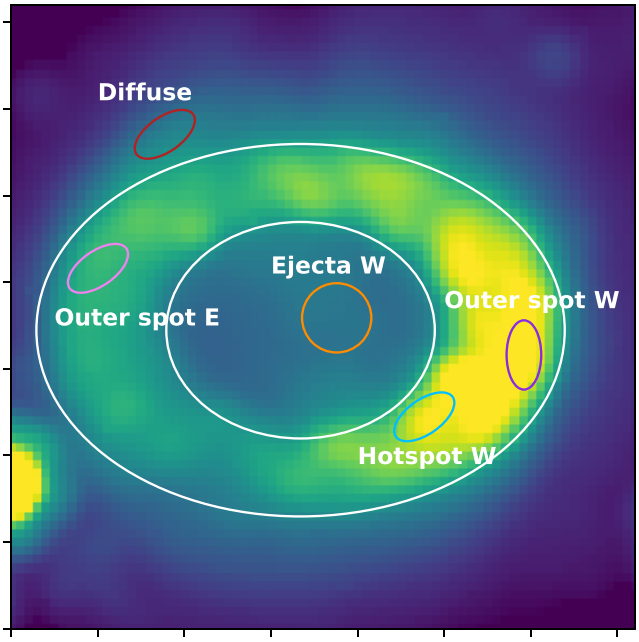

Figure 10. Small regions (in colour) used for SEDs in Fig. 11 and the white elliptical annuals used for the ring and outer spots photometry in Fig. 12 (also in Appendix B), overlaid on *F323N* image.

3.3 Power-law spectra at 3–4 μm in the equatorial ring and its exterior

In order to understand the nature of emitting sources, we measure the SEDs within several apertures across SN 1987A. The locations of apertures are marked in Fig. 10, and the extracted SEDs are plotted in Fig. 11. The 'background' or ISM continuum level, which is estimated from the nearby field (Section 2), has been subtracted beforehand.

The fluxes at *F323N*, *F356W*, and *F444W* follow a power-law continuum across SN 1987A (black lines in Fig 11). The ejecta have the steepest power-law index α at a value of 3.1, where α

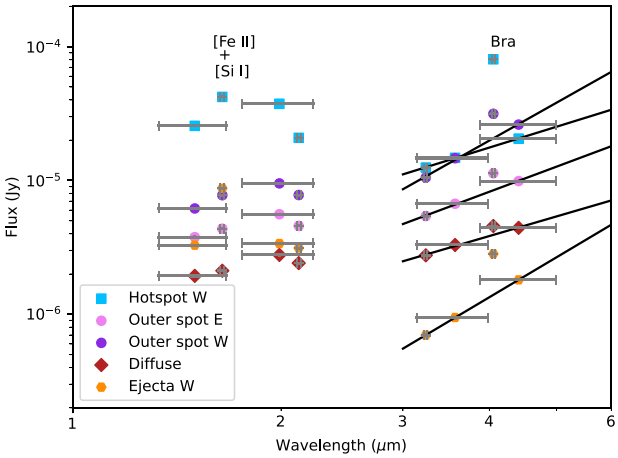

Figure 11. The spectra at represented regions indicated in Fig. 10. The black lines are power-law fits to the *F323N*, *F356W*, and *F444W* fluxes and the grey horizontal lines show the filter widths. The uncertainties of the fluxes are smaller than the plotting symbols.

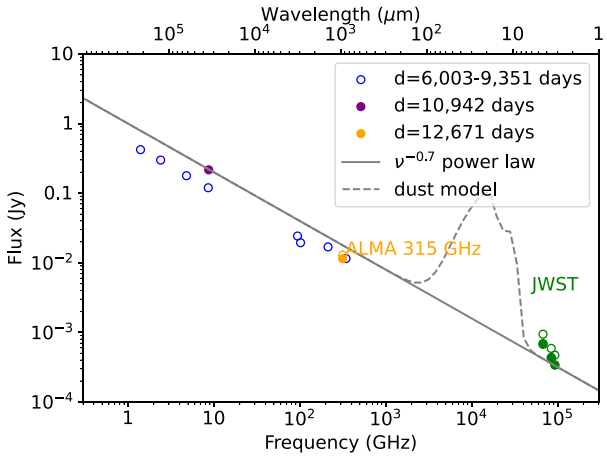

Figure 12. The SEDs from NIR to radio in the past 2 yr and the past. The filled circles of ALMA and *JWST*/NIRCam data points show the fluxes of the equatorial ring and the outer spots. For *JWST*/NIRCam, additionally the diffuse emission is included in the fluxes plotted with empty circles. The grey dashed line shows the 'warm' dust model from Matsuura et al. (2022).

is defined as $F_\nu \propto \nu^{-\alpha}$. Apart from the ejecta, as expected from the $I_{\nu\,\mathrm{F444W}}/I_{\nu\,\mathrm{F356W}}$ ratio map in Fig. 6, the steepest power-law index is found on the western side of the outer spots. The power-law indices are $\alpha = 2.9$ and 1.9 at the western and eastern outer spots, respectively. The power-law indices are as small as $\alpha = 1.6$ at the hotspots on the ring and $\alpha = 1.5$ within the diffuse emission.

3.3.1 *NIR continuum: synchrotron and dust*

In light of the power-law SEDs in the 3–4 μm wavelength range, we discuss the sources of this emission in the equatorial ring and its exterior. Historically, the emission at 3–4 μm was solely attributed to dust thermal emission from the equatorial ring, but synchrotron emission can be an additional and important source at the current epoch. In shocked gas, fast-moving electrons collide with dust grains and collisionally heated dust grains, which have a temperature of 180–200 K (Dwek et al. 2010; Matsuura et al. 2018), and radiate their energy at the MIR wavelengths (Fig. 12). The modified blackbody emission from the warm dust drops sharply from the SED peak towards NIR wavelengths, in accordance with the Wien's law approximation to the Planck function. Thus, NIR emission has been explained by additional 'hot' (370–460 K; Dwek et al. 2010) dust consisting of smaller grains. Because the heat capacities of small grains are lower, they can reach much higher energy than the larger grains.

On the other hand, our total SED analysis suggests that synchrotron emission can contribute substantially to the NIR flux in the ring and its exterior. Fig. 12 shows the integrated SED of the ring and outer hotspots from the IR to the millimetre wavelengths. The total fluxes in the *JWST F323N*, *F356W*, and *F444W* bands are plotted in open green circles, where the aperture sizes are described in Appendix. B. The historical measurements of the radio synchrotron emission before 2014 are plotted in blue circles, and they demonstrate the power law of the synchrotron emission (Zanardo et al. 2010, 2013, 2014). The day 10 942 flux measurement at 8.7 GHz from Cendes et al. (2018) is plotted with the filled purple circle. The total ALMA 315 GHz flux in 2021 is plotted with an orange open circle and the flux excluding the ejecta is plotted in a filled orange circle. The radio fluxes continued to increase since 2014 until at least until 2017 (Cendes et al. 2018), so that pre-2014 fluxes are lower than the latest (day = 10 942) flux measurement at 8.7 GHz (Cendes et al. 2018). The power-law index at the millimetre and submillimetre wavelengths has been estimated as $\alpha = 0.74$ by Zanardo et al. (2013), fitting the blue open circles. More recently, Cigan et al. (2019) estimated $\alpha = 0.70$.

In Fig. 12, the grey line shows the power law of $\alpha = 0.70$ crossing the 8.7 GHz flux at day = 10 942. Even though it is not intended to fit the *JWST* fluxes, the grey line can explain the *F323N* and *F356W* fluxes very well, showing that a substantial fraction of the NIR fluxes is synchrotron emission. The ALMA flux at 315 GHz is probably underestimated, because the interferometry had a fully recoverable size of only 0.99 arcsec, and any structure extending beyond that size, such as diffuse emission, is over-resolved and its flux is not properly accounted.

Similar analysis of the *JWST* NIRSpec and MIRI/MRS total SED also found that synchrotron radiation is the most important source of the continuum in the 3–4 μm range (Jones et al. 2023). Hot (~300 K) dust starts to contribute to *F444W*, only.

In other young SNRs, Cassiopeia A and the Crab Nebula, the synchrotron emission contributes to the continuum emission from IR wavelengths at 2 μm to cm wavelengths (Jones et al. 2003; Gomez et al. 2012; Domček et al. 2021). It is not surprising synchrotron emission contributes to the continuum in SN 1987A, too.

Jones et al. showed that the total SED of SN 1987A at 3–4 μm additionally contains minor contributions from free–free and bound–free emission. However, their flux density decreases at longer wavelengths, which is opposite to the increasing continuum with longer wavelengths in the measured spectra. Hence, the contributions of free–free and bound–free emissions into the 3–4 μm spectra are likely very minor.

3.3.2 *Spatial distributions of dust and synchrotron*

Now, we carefully examine the spatial distributions of dust and synchrotron emission.

The *F356W* image is compared with the ALMA continuum image in Fig. 8 (right panel). The ALMA continuum image traces synchrotron in the ring and its exterior, though it does trace dust in the ejecta. In 2021, the emitting regions of the ALMA 315 GHz

(950 μm) flux correspond to hotspots within the equatorial ring and the outer spots exterior to the equatorial ring (Fig. 8). In particular, on the eastern side, the 315 GHz emission is found mostly in the outer spots, and hardly found in the hotspots.

Fig. 13 compares the *F356W* image and dust continuum image. The left top panel of the figure shows the *F164N* image, and contours of the *F164N* image are plotted in the other three panels in order to guide the locations of hotspots and diffuse emission. The lower panels are MIRI/MRS images, replicated from Jones et al. (2023). The left lower panel shows H I 7.46 μm image, demonstrating that ionized gas is emitted from the hotspots but only weakly from the outer spots, similar to *F164N* ring image. In contrast, the 7.4436–7.4572 μm dust image (the right lower panel) reveals that the dust emission is from the exterior to the equatorial ring, that is, either outer spots or diffuse component. These outer spots and diffuse emission have the steepest power-law index at *F444W*/*F356W* (Fig. 6). The dust thermal emission at $\lesssim 7$ μm corresponds to the Wien's law regime of the blackbody, which can explain a steep ($\alpha \sim 3$; Fig. 11) power-law index. The brightest hotspots within the western ring in *F356W* image (right top panel) have little dust emission at the 7 μm continuum (right bottom panel), hence, these hotspots are most likely synchrotron-dominated.

There is a morphological difference amongst dust, synchrotron, and atomic lines (Hα and [Fe II]): dust emission appears at the limited locations of the diffuse emission and outer spots, while synchrotron emission is found in both outer spots and hotspots, as well as diffuse emission. Hα and [Fe II]emission is strongest at the hotspots. The difference in emitting locations is caused by the time-scale of these three physical processes. More narrowly confined dust emitting regions in comparison with synchrotron emitting regions is explained by the shorter cooling time-scale of dust grains than synchrotron electrons in the post-shocked region. The radially expanding shocks gradually engulf new circumstellar material, including dust grains. Fast-moving electrons in hot shocked gas collide with dust grains, heating these grains. The heated grains emit the NIR and MIR and radiation, which also cools down dust grains and gas in post-shocked regions. Further, a high collision of charged particles can sputter atoms from the surface of dust grains, and making dust grain size smaller (dust destruction). The cooling time-scale was predicted to be 12–22 yr at a gas density of $n_{\rm H} = 10^4$ cm^{-3} for grain sizes of >0.2 μm, and at a post-shock velocity of 600–700 km s^{-1}. Smaller grains cool faster than that. Whereas the dust destruction time-scale was predicted to be 4–15 yr (Dwek et al. 2010). Overall the shocks have passed the equatorial ring after about 2010 (Fransson et al. 2015), although the western side of the ring seems to have interacted until about 2014 (Larsson et al. 2019). Little dust emission from the hotspots within the equatorial ring in 2022 shows that either the cooling time-scale or destruction time-scale of dust grains is less than 8 yr. If the cooling rate is responsible for fading MIR dust emission, the grain size can be smaller than 0.2 μm. Otherwise, dust grains in the hotspots are destroyed, hence, little emission is left at the hotspots.

On the other hand, the radiative loss time-scale of relativistic electrons may be longer than the 10-yr time-scale, as discussed in the next section, hence, synchrotron radiation is still emitted in hotspots, even if the shocks have passed 12 yr ago.

The brightness of the hydrogen recombination lines also changes within the recombination time-scale, which is $\tau = (\alpha_B n_{\rm H})^{-1} = 1.22 \times 10^5 / n_{\rm H}$ yr (eq. 15.7 of Draine 2011), where $n_{\rm H}$ is the hydrogen number density in cm^{-3}. With estimated density of $n_{\rm H} = 10^4$ cm^{-3}, the recombination time-scale is 12 yr. Having Hα in the western hotspots still but gradually fading since 2014 matches with explanation by this recombination time-scale.

3.3.3 Broken power-law synchrotron emission at NIR wavelengths

Synchrotron radiation makes a substantial contribution to the NIR continuum. The NIR power-law index of the continuum is about α=1.5–1.6 at hotspots. This is higher than the millimetre power-law index, measured to be $\alpha = 0.7$–0.74 (Zanardo et al. 2013; Cigan et al. 2019). Having little MIR dust emission at hotspots, it is very unlikely that the tail of dust emission increases the power law at hotspots. The synchrotron power-law index at NIR wavelengths is likely to be intrinsically higher than that at millimetre wavelengths at hotspots.

Though synchrotron radiation, in general, follows a power law ($F_\nu \propto \nu^{-\alpha}$), the radiative lifetime of the more energetic electrons, which are responsible of the emission at higher frequencies, is shorter, leading to a steepening of the spectrum at higher frequencies (Ginzburg & Syrovatskii 1965; Longair 2011; Domček et al. 2021). The breakpoint of the power-law index is in general found at optical and mid-IR wavelengths in SN remnants (Bühler & Blandford 2014; Domček et al. 2021). Having a broken law in the IR wavelengths may explain the steeper NIRCam power-law index than that in the millimetre wavelength.

Moreover, previous millimetre power-law index measurements suggest the synchrotron power-law index itself could have some spatial variations; $\alpha = 0.6$–1.0 with an aperture of 0.8 arcsec (Zanardo et al. 2014).

We test if such a broken IR law of the synchrotron emission is feasible in SN 1987A. If a relativistic electron can lose energy by synchrotron radiation before an electron accelerates to that energy (or frequency), there is no electron emitting synchrotron radiation at that frequency. The typical frequency, $\nu_{\rm br}$, where radiative loss affects the spectrum is given by

$$\nu_{\rm br} \approx 7.2 \times 10^{16} \left(\frac{B}{100\,\mu{\rm G}} \right)^{-3} \left(\frac{t_{\rm age}}{100\,{\rm yr}} \right)^{-2} {\rm Hz}, \quad (1)$$

where B is the magnetic field, and $t_{\rm age}$ is the electron's radiative lifetime (Domček et al. 2021, also in Pacholczyk 1970). The collision of the blast wave with the equatorial ring occurred somewhere between 1999 and 2005 (Luo & McCray 1991; Chevalier & Dwarkadas 1995; McCray & Fransson 2016), so that the lifetime should be less than 27 yr. Having the break wavelength/frequency to be at 3 μm requires the magnetic field of $B \geq 2.1$ mG. The polarization measurement of the millimetre synchrotron emission estimated the magnetic field of a few mG at the post-shocked region in 2015–2016 (Zanardo et al. 2018). This magnetic field can cause a broken power-law index of the synchrotron emission.

Theoretical models of SN shock evolution show a broken power law in the presence of a strong magnetic field. Berezhko, Ksenofontov & Völk (2011) predicted the broken law to be present at IR wavelengths in SN 1987A. The model involved a 20 mG magnetic field downstream, as this could explain non-detection of synchrotron emission in X-ray in their model. In this case, the synchrotron broken law already appears at the MIR, and continues with the steep power-law index into the NIR. The predicted spectra had time variation, and the IR power-law index of about 1.2 was predicted in 2020. This predicted index is slightly smaller than the observed one, but much steeper than the millimetre power-law index. On the other hand, Petruk et al. (2023) predicted a much lower magnetic field (<20 μG), and in this case, the power-law break falls at a shorter

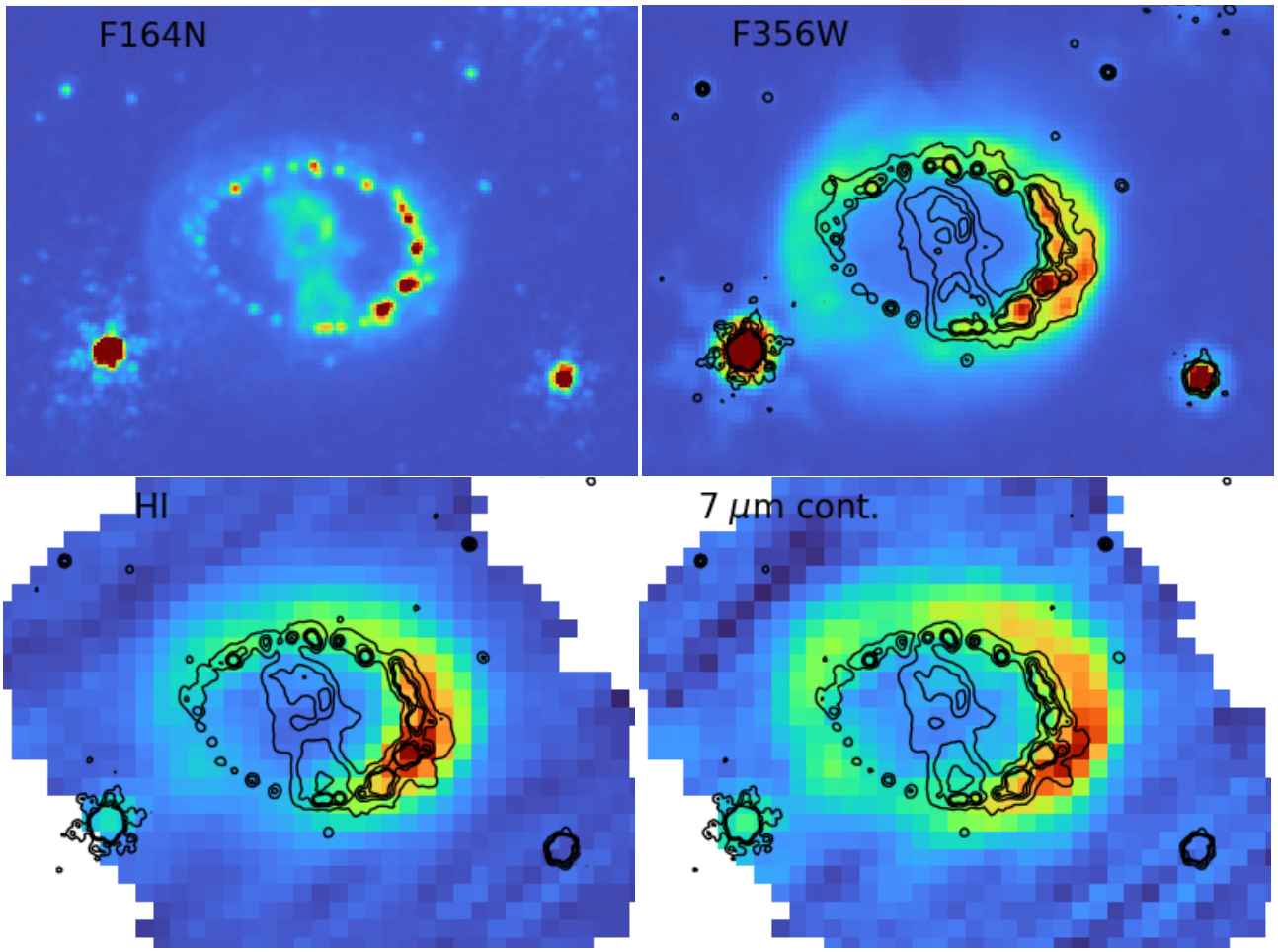

Figure 13. Comparison of the emitting regions of ionized gas (*F164N* and 7.46 μm H I 6–5 Pfα lines), *F356W* continuum and 7 μm (7.43–7.45 μm) continuum. The 7.46 μm H I 6–5 Pfα lines and 7 μm continuum images are from MIRI/MRS, replicated from Jones et al. (2023). The black contour lines trace *F164N*, though due to slightly different smoothing of the *F164N* data to the new pixel scales, there is a subtle difference in contour lines from one image to the other. The dust continuum, represented by the 7 μm continuum, is mainly emitted from outer spots and diffuse emission, while *F356W* emission is found in both hotspots and outer spots, as well as diffuse emission.

wavelength than the NIR. These contrasting predictions show that the measurement of a magnetic field is the key next step.

3.3.4 The NIR continuum as a tracer of shocks and ionized lines as a tracer of recombining regions

Historically, synchrotron emission, detected in radio and X-ray wavelengths, was found only from the equatorial ring, and the outer spots were not considered (e.g. Park et al. 2002; Ng et al. 2013; Zanardo et al. 2014). That was definitely the case at least until about 2014, when the blast waves were about to pass the equatorial ring (Fransson et al. 2015). Although not fully resolved down to the scale of the hotspots and outer spots, the radii of the radio and the X-ray emitting ring sizes have continued to increase since then (Frank et al. 2016; Cendes et al. 2018). This trend is more prominent in the hard (0.5–10 k eV) X-ray emission. The soft (0.3–0.8 keV) X-ray emission radius stagnated around day 6000 in 2004 (Frank et al. 2016), and it is considered to be from hotspots in the equatorial ring (Dewey et al. 2012). In the ALMA image taken in 2015, the synchrotron emission extended just beyond the equatorial ring (Cigan et al. 2019).

Now, the synchrotron emission in X-ray and radio wavelengths must be emitted by both the ring hotspots and the outer spots, as shown by the *JWST F323N*, *F356W*, and *F444W* images and the ALMA 315 GHz image. That would explain the recent increase in the radii of the radio and hard X-ray emission. Considering that the brightness from the west side of the equatorial ring and outer spots dominates the overall brightness in the *F323N*, *F356W*, *F444W*, and radio flux, as well as X-ray, the current interactions of shocks with the circumstellar material must be dominant on the western side of the equatorial ring and the material beyond the ring. The majority of the blast waves have already passed the equatorial ring on the eastern side.

Shocked gas is typically traced by X-rays, and the electron temperature is estimated to be 1–3 $\times$ 10^7 K (Ravi et al. 2021). Around that temperature, in case A, hydrogen recombination lines have emissivity decreasing with increasing temperature, as $T^{-0.92}$ (Storey & Hummer 1995). The outer spots, where current interaction is ongoing, are expected to have a higher temperature than the 'hotspots' (Note that the name of 'hotspots' is based on observations in 1990s and the temperature has changed since, and does not reflect the current temperature.). This explains why hotspots are brighter than the outer spots in hydrogen recombination lines, such as Brα ($I_{\nu\,\mathrm{F405N}}$ in Fig. 5) and *HST* Hα images (Larsson et al. 2019). That makes the contrast between the hydrogen recombination

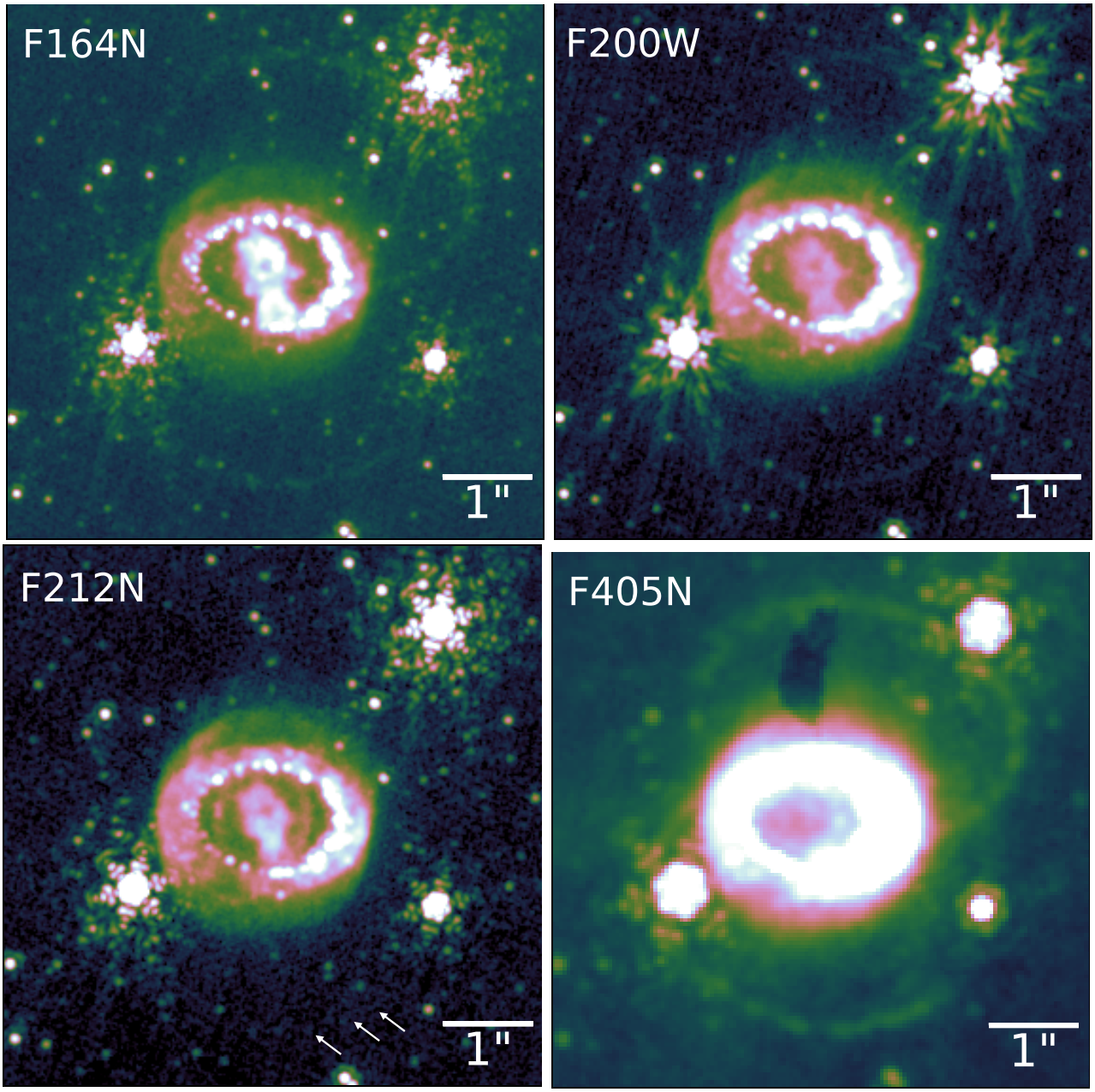

Figure 14. The detection of the outer rings in four filter bands. The arrows in the *F212N* image show the locations of potential detections of the outer rings. The black shadow in the *F405N* is an artefact, due to incomplete flat-field correction.

line images, which show the hotspots to be brighter than the outer spots, and the continuum images (*JWST F323N*, *F356W*, and *F444W* images), which have equally bright hotspots and outer spots.

The continuum may contain some emission from small dust grains (Dwek et al. 2008; Matsuura et al. 2022; Arendt et al. 2023; Jones et al. 2023). The emission is from collisionally heated dust in shocks. Even if arising from a combination of synchrotron and dust emission, the power-law continuum emission in the NIR wavelength would be a good tracer of the shocked region.

In contrast, the ionized lines originate from hotspots within the equatorial ring, which contain more substantial gas mass but have lower temperatures. The recombination time-scale is much longer than the synchrotron cooling time, and a lower temperature favours higher recombination line emissivity. The hotspots within the equatorial ring thus remain brighter for longer time-scales in recombination lines.

3.4 Outer rings

The outer rings are considered to have been expelled from the progenitor about 20 000 yr before the SN explosion (Panagia et al. 1996; Crotts & Heathcote 2000). The outer rings have been detected mainly in atomic lines, such as [N II], [O III], and Hα in the optical wavelengths (Panagia et al. 1996; Tziamtzis et al. 2011), and Ne and [O I] lines in the MIR wavelengths (Jones et al. 2023).

In our NIRCam images, very faint emission from the outer rings was detected in three filter bands *F164N*, *F200W*, and *F405N*

(Fig. 14). All three filter bandpasses contain atomic lines: *F164N* contains 1.641 μm and [Fe II] line, *F200W* is mainly from 1.875 μm Paα, and 2.059 μm He I lines, and *F405N* is from Brα. A hint of part of the outer rings is recognizable in the *F212N* image, too. Non-detections in the continuum-dominated filters may suggest that the emission from the outer rings is dominated by the atomic lines with very faint H_2 in *F212N*. This supports the proposition that the gas in the outer rings was ionized by the initial SN flash (Tziamtzis et al. 2011) and that lines from the ionized gas can be still detected at this late epoch.

The outer rings are known to cross the ejecta and the equatorial ring as seen in projection from Earth (Tziamtzis et al. 2011). We assess if the emission from the outer rings may still contribute to some structures in the *JWST* image in 2022 in Appendix A. From the measurement of the surface brightness, the outer ring emission accounts for a negligible fraction (less than 10 per cent) of the surface brightness of the ejecta in *F164N* and *F200W* images.

4 CONCLUSIONS

Very deep and high angular resolution NIRCam imaging of SN 1987A reveals unprecedented details of NIR emission from this young SN remnant. This includes the detection of the NIR synchrotron emission, the discovery of the crescents, and the characterization of the bar, which is a substructure of the ejecta.

Regions currently undergoing shocks are traced by the NIR continuum through synchrotron and thermal dust emission at 3–5 µm. This continuum emission is spatially resolved in NIRCam images, and is found in hotspots within the equatorial ring, in outer spots exterior to the equatorial ring, as well as in the diffuse emission exterior to the equatorial ring. At 3–5 µm, the outer spots are as bright as the hotspots, despite the fact that the hotspots have the highest density within the circumstellar system. This is probably because stronger magnetic fields and enhanced local density at shocks increase the synchrotron radiation in the outer spots. Future monitoring and modelling of synchrotron emission will reveal how the synchrotron emission evolves with time in an SNR, after the passage of the shock front. Such time sequence observations will provide a rare opportunity amongst SNRs that would constrain hydrodynamic models of SN shocks (e.g. Borkowski, Blondin & McCray 1997; Dewey et al. 2012; Kirchschlager et al. 2019; Orlando et al. 2020), and particle acceleration in the shocked regions (e.g. Domček et al. 2021). With the advent of high sensitivity and high angular resolution images provided by *JWST*/NIRCam, our observations of SN 1987A demonstrate that NIRCam opens up a window to study particle-acceleration physics probed by NIR synchrotron emission in SN remnants and other synchrotron emitting objects such as active galactic nuclei and blazars.

The NIRCam 1–2 μm images reveal the clumpy structure of the ejecta, including the bar. The presence of clumpy structure is consistent with SN explosion models that predict the fragmentation of the SN ejecta into clumps due to Rayleigh–Taylor instabilities, which are triggered by the explosions (Wongwathanarat, Muller & Janka 2015).

The NIRCam images show that the centre of the ejecta is still obscured by dust, and seen as a 'hole' at the 3–5 µm wavelengths. The presence of dust obscuration in the ejecta means that optical and NIR emission mainly traces the foreground of this heavily self-absorbed dusty region. As this heavily self-absorbed dust region expands further, the optical depth of the dust will decrease in time. Once the dust optical depth has dropped sufficiently, a complete picture of the ejecta will be visible at the NIR wavelengths. A new feature, the crescents, is discovered between the ejecta and the equatorial ring. The crescents are probably either the ionization front of the inner ejecta, irradiated by X-ray and UV emitted from the outer spots, or the edge of the reverse shocks bounced back from the equatorial ring. Details of our analysis of these crescents will be published elsewhere.

Very deep and high angular resolution NIRCam images revealed detailed structures in the young and close SNR, SN 1987A. They will be used to understand the physical processes that shape complex structures of SNe. The processes to be investigated include mass loss from the progenitor star, the SN explosion, dynamical processes, heating (by X-ray and UV radiation, and ^{44}Ti decay, and potentially the neutron star) and cooling processes (atomic and dust radiations, as well as adiabatic). All of these processes are imprinted into the complexity of emissions from the ejecta and circumstellar matter in this SNR. The next stage is to disentangle all of these processes to truly understand the cause of the complexity and time evolution of the SNRs.

ACKNOWLEDGEMENTS

This work is based on observations made with the NASA/ESA/CSA *JWST*. The data were obtained from the Mikulski Archive for Space Telescopes at the Space Telescope Science Institute, which is operated by the Association of Universities for Research in Astronomy, Inc., under NASA contract NAS 5–03127 for *JWST*. These observations are associated with program no. 1726.

This paper makes use of the following ALMA data: ADS/JAO.ALMA#2021.1.00707.S. ALMA is a partnership of ESO (representing its member states), NSF (USA), and NINS (Japan), together with NRC (Canada), MOST and ASIAA (Taiwan), and KASI (Republic of Korea), in cooperation with the Republic of Chile. The Joint ALMA Observatory is operated by ESO, AUI/NRAO and NAOJ.

This work also utilizes *JWST* data from the program no. 1232, obtained from the Mikulski Archive.

This work presents results from the European Space Agency (ESA) space mission *Gaia*. *Gaia* data are being processed by the Gaia Data Processing and Analysis Consortium (DPAC). Funding for the DPAC is provided by national institutions, in particular the institutions participating in the Gaia MultiLateral Agreement (MLA).

MM and RW acknowledge support from the STFC Consolidated grant (ST/W000830/1). MJB and RW acknowledge support from European Research Council (ERC) advanced grant SNDUST 694520. IDL and FK acknowledge funding from the European Research Council (ERC) under the European Union's Horizon 2020 research and innovation programme (no. 851622 DustOrigin). RDG was supported, in part, by the United States Air Force. Work by RGA was supported by NASA under award no. 80GSFC21M0002. APR and SP are supported in part by the STScI grant, JWST-GO-01726.032-A. CG is supported by a Villum FondeN Young Investigator Grant (project no. 25501).

DATA AVAILABILITY

The pipeline reduced data are available at MIKULSKI archive (http://dx.doi.org/10.17909/dzkq-7c90).

REFERENCES

Aniano G., Draine B. T., Gordon K. D., Sandstrom K., 2011, PASP, 123, 1218

Arendt R. G., Dwek E., Bouchet P., Danziger I. J., Frank K. A., Gehrz R. D., Park S., Woodward C. E., 2016, AJ, 151, 62
Arendt R. G., Dwek E., Bouchet P., Danziger I. J., Gehrz R. D., Park S., Woodward C. E., 2020, ApJ, 890, 2
Arendt R. G., et al., 2023, ApJ, 959, 95
Arnett W. D., Bahcall J. N., Kirshner R. P., Woosley S. E., 1989, ARA&A, 27, 629
Berezhko E. G., Ksenofontov L. T., Völk H. J., 2011, ApJ, 732, 58
Black J. H., van Dishoeck E. F., 1987, ApJ, 322, 412
Borkowski K. J., Blondin J. M., McCray R., 1997, ApJ, 477, 281
Bouchet P., et al., 2006, ApJ, 650, 212
Brandner W., Chu Y.-H., Eisenhauer F., Grebel E. K., Points S. D., 1997, ApJ, 489, L153
Bühler R., Blandford R., 2014, Rep. Prog. Phys., 77, 066901
Bushouse H. et al., , 2023, JWST Calibration Pipeline, Zenodo
Cendes Y., Gaensler B. M., Ng C.-Y., Zanardo G., Staveley-Smith L., Tzioumis A. K., 2018, ApJ, 867, 65
Chevalier R. A., Dwarkadas V. V., 1995, ApJ, 452, L45
Cigan P., et al., 2019, ApJ, 886, 51
Crotts A. P., Heathcote S. R., 1991, Nature, 350, 683
Crotts A. P. S., Heathcote S. R., 2000, ApJ, 528, 426
Crotts A. P. S., Kunkel W. E., Heathcote S. R., 1995, ApJ, 438, 724
Dewey D., Dwarkadas V. V., Haberl F., Sturm R., Canizares C. R., 2012, ApJ, 752, 103
Domček V., Vink J., Hernández Santisteban J. V., DeLaney T., Zhou P., 2021, MNRAS, 502, 1026
Draine B. T., 2011, Physics of the Interstellar and Intergalactic Medium. Princeton University Press, Princeton, NJ
Dwek E., et al., 2008, ApJ, 676, 1029
Dwek E., et al., 2010, ApJ, 722, 425
Eisenhauer F., et al., 2003, in Iye M., Moorwood A. F. M.eds, Proc. SPIE Conf. Ser. Vol. 4841, Instrument Design and Performance for Optical/Infrared Ground-based Telescopes. SPIE, Bellingham, p. 1548
France K., et al., 2015, ApJ, 801, L16
Frank K. A., Zhekov S. A., Park S., McCray R. A., Dwek E., Burrows D. N., 2016, ApJ, 829, 40
Fransson C., Cassatella A., Gilmozzi R., Kirshner R. P., Panagia N., Sonneborn G., Wamsteker W., 1989, ApJ, 336, 429
Fransson C. et al., 2013, ApJ, 768, 88
Fransson C., Larsson J., Migotto K., et al., 2015, ApJ, 806, L19
Gaia Collaboration, 2018, A&A, 616, A1
Gardner J. P. et al., 2023, PASP, 135, 1048
Ginzburg V. L., Syrovatskii S. I., 1965, ARA&A, 3, 297
Gomez H. L. et al., 2012, ApJ, 760, 96
Gordon K. D., Engelbracht C. W., Rieke G. H., Misselt K. A., Smith J. D. T., Kennicutt Robert C. J., 2008, ApJ, 682, 336
Greenhouse M. A., Woodward C. E., Thronson Harley A. J., Rudy R. J., Rossano G. S., Erwin P., Puetter R. C., 1991, ApJ, 383, 164
Harris F., 1978, Proc. IEEE, 66, 51
Indebetouw R. et al., 2014, ApJ, 782, L2
Jakobsen P. et al., 1991, ApJ, 369, L63
Jerkstrand A., Fransson C., Kozma C., 2011, A&A, 530, A45
Jones T. J., Rudnick L., DeLaney T., Bowden J., 2003, ApJ, 587, 227
Jones O. C. et al., 2023, ApJ, 958, 95
Kangas T. et al., 2022, MNRAS, 511, 2977
Kirchschlager F., Schmidt F. D., Barlow M. J., Fogerty E. L., Bevan A., Priestley F. D., 2019, MNRAS, 489, 4465
Kjær K., Leibundgut B., Fransson C., Gröningsson P., Spyromilio J., Kissler-Patig M., 2007, A&A, 471, 617
Larsson J. et al., 2013, ApJ, 768, 89
Larsson J. et al., 2016, ApJ, 833, 147
Larsson J. et al., 2019, ApJ, 886, 147
Larsson J. et al., 2023, ApJ, 949, L27
Lawrence S. S., Sugerman B. E., Bouchet P., Crotts A. P. S., Uglesich R., Heathcote S., 2000, ApJ, 537, L123
Lloyd H. M., O'Brien T. J., Kahn F. D., 1995, MNRAS, 273, L19
Longair M. S., 2011, High Energy Astrophysics. Cambridge University Press, Cambridge, UK
Luo D., McCray R., 1991, ApJ, 379, 659
Matsuura M. et al., 2011, Science, 333, 1258
Matsuura M. et al., 2015, ApJ, 800, 50
Matsuura M. et al., 2018, MNRAS, 482, 1715
Matsuura M. et al., 2022, MNRAS, 517, 4327
McCray R. A., 1993, ARA&A, 31, 175
McCray R., 2003, in Weiler K.ed., Supernovae and Gamma-Ray Bursters, Vol. 598. Springer-Verlag, Berlin Heidelberg, p. 219
McCray R. A., Fransson C., 2016, ARA&A, 54, 19
Meaburn J., Bryce M., Holloway A. J., 1995, A&A, 299, L1
Morris T., Podsiadlowski P., 2007, Science, 315, 1103
Mouri H., Kawara K., Taniguchi Y., 2000, ApJ, 528, 186
Ng C.-Y., Zanardo G., Potter T. M., Staveley-Smith L., Gaensler B. M., Manchester R. N., Tzioumis A. K., 2013, ApJ, 777, 131
Orlando S. et al., 2020, A&A, 636, A22
Pacholczyk A. G., 1970, Radio Astrophysics. Nonthermal Processes in Galactic and Extragalactic Sources. W. H. Freeman and Co., San Francisco
Panagia N., Scuderi S., Gilmozzi R., Challis P. M., Garnavich P. M., Kirshner R. P., 1996, ApJ, 459, L17
Park S., Burrows D. N., Garmire G. P., Nousek J. A., McCray R., Michael E., Zhekov S., 2002, ApJ, 567, 314
Perrin M. D., Sivaramakrishnan A., Lajoie C.-P., Elliott E., Pueyo L., Ravindranath S., Albert L., 2014, in Oschmann Jacobus M. J., Clampin M., Fazio G. G., MacEwen H. A.eds, Proc. SPIE Conf. Ser. Vol. 9143, Space Telescopes and Instrumentation 2014: Optical, Infrared, and Millimeter Wave. SPIE, Bellingham, p. 91433X
Petruk O. et al., 2023, MNRAS, 518, 6377
Phillips M. M., Heathcote S. R., Hamuy M., Navarrete M., 1988, AJ, 95, 1087
Pietrzyński G. et al., 2019, Nature, 567, 200
Ravi A. P., Park S., Zhekov S. A., Miceli M., Orlando S., Frank K. A., Burrows D. N., 2021, ApJ, 922, 140
Raymond J. C., Koo B.-C., Lee Y.-H., Milisavljevic D., Fesen R. A., Chilingarian I., 2018, ApJ, 866, 128
Rieke M. J. et al., 2023, PASP, 135, 028001
Rigby J. et al., 2023, PASP, 135, 1046
Roueff E., Abgrall H., Czachorowski P., Pachucki K., Puchalski M., Komasa J., 2019, A&A, 630, A58
Saio H., Nomoto K., Kato M., 1988, Nature, 334, 508
Shull J. M., Steenberg M. v., 1982, ApJS, 48, 95
Smith N., 2007, AJ, 133, 1034
Smith N., Bally J., Walawender J., 2007, AJ, 134, 846
Smith N., Arnett W. D., Bally J., Ginsburg A., Filippenko A. V., 2013, MNRAS, 429, 1324
Sonneborn G. et al., 1998, ApJ, 492, L139
Storey P. J., Hummer D. G., 1995, MNRAS, 272, 41
Tokunaga A. T., Vacca W. D., 2005, PASP, 117, 421
Tziamtzis A., Lundqvist P., Groningsson P., Nasoudi-Shoar S., 2011, A&A, 527, A35
Wongwathanarat A., Muller E., Janka H. T. T., 2015, A&A, 577, A48
Zanardo G. et al., 2010, ApJ, 710, 1515
Zanardo G., Staveley-Smith L., Ng C.-Y., Gaensler B. M., Potter T. M., Manchester R. N., Tzioumis A. K., 2013, ApJ, 767, 98
Zanardo G. et al., 2014, ApJ, 796, 82
Zanardo G., Staveley-Smith L., Gaensler B., Indebetouw R., Ng C.-Y., Matsuura M., Tzioumis A. K., 2018, ApJ, 861, L9

APPENDIX A: CONTRIBUTION OF THE OUTER RING ONTO THE EJECTA

The outer rings are known to cross the ejecta and the equatorial ring as seen in projection from Earth (Tziamtzis et al. 2011). We assess if the emission from the outer rings may still contribute to some structures in the *JWST* image in 2022. The outer rings have been gradually fading since the *HST* image was taken in 2003 (Tziamtzis et al. 2011), and we use the 2003 *HST* image as a guide of the outer ring, rather than more recent *HST* images. The left panel of Fig. A1

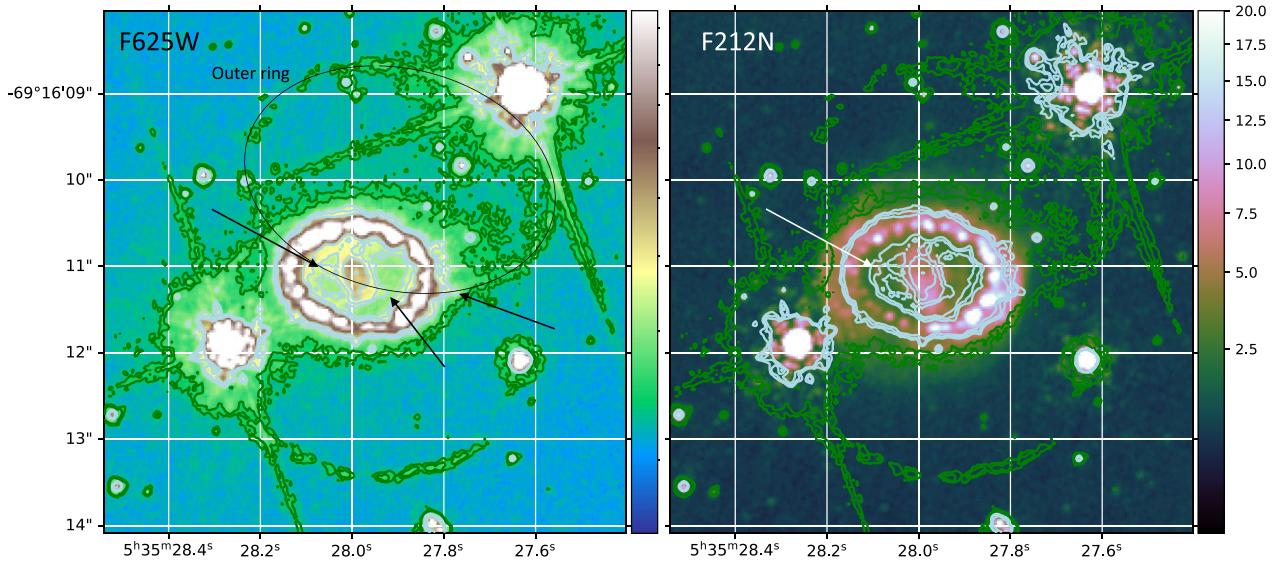

Figure A1. Left: *HST F625W* image in 2003 (Tziamtzis et al. 2011), showing the outer rings in the line contours. The north outer ring crosses the equatorial ring and ejecta, indicated by three black arrows. Since then, the outer ring has faded gradually. Right: *F212N* image in colour contours, overlayed with line contours identical to the left panel (green and white). The colour bar is in the unit of MJy sr^{-1}. The local peak on the east crescent could have some gain of the surface brightness from the outer rings.

shows the *HST F625W* image. The levels of the line contours are adjusted to highlight the outer rings, the equatorial ring and the ejecta. The northern outer ring is encircled with a black line. This ring is highlighted at three locations using black arrows: the ring enters the equatorial ring from the north-east, and proceeds towards the centre of the equatorial ring, then exits from the south-west of the ejecta. Afterwards, it crosses the equatorial ring for the second time. Grey contour lines show some local increase in intensities at these three locations. The right panel of Fig. A1 shows the NIRCam *F212N* image of the same region in the colour contour. The line contours are taken from the *HST F625W* image. At the position of the white arrow, the north outer ring and the east crescent meet. This crossing point coincides with the local peak of the crescent. This local peak might have some gain in the intensity from the outer ring. Alternatively, the colour seems to be blue, which might be a sign of a field star at this location. From the measurement of the surface brightness, the outer ring emission accounts for a negligible fraction (less than 10 per cent) of the surface brightness of the ejecta in *F164N* and *F200W* images.

APPENDIX B: MEASUREMENTS OF THE FLUXES IN THE EQUATORIAL RING AND OUTER SPOTS

In order to measure the NIR continuum fluxes in the equatorial ring and outer spots, two different types of elliptical apertures were used. These fluxes were measured with an elliptical aperture of 1.50 and 1.37 arcsec major and minor axes (Fig. 10), with a negligible contribution from field stars within the aperture. The filled circles show the fluxes measured from another elliptical annulus that includes the ring and the outer spots, but excludes the ejecta and diffuse emission outside the outer spots. The major axes of the inner and outer annulus are 0.65 and 1.28 arcsec and minor axes of these are 0.52 and 0.90 arcsec.

[1]*Cardiff Hub for Astrophysical Research and Technology (CHART), School of Physics and Astronomy, Cardiff University, The Parade, Cardiff CF24 3AA, UK*
[2]*Space Telescope Science Institute, 3700 San Martin Drive, Baltimore, MD 21218, USA*
[3]*Observational Cosmology Lab, Code 665, NASA Goddard Space Flight Center, Greenbelt, MD 20771, USA*
[4]*Center for Space Sciences and Technology, University of Maryland, Baltimore County, Baltimore, MD 21250, USA*
[5]*Department of Physics, KTH Royal Institute of Technology, The Oskar Klein Centre, AlbaNova, Stockholm SE-106 91, Sweden*
[6]*Department of Astronomy, Stockholm University, The Oskar Klein Centre, AlbaNova, Stockholm SE-106 91, Sweden*
[7]*Department of Physics and Astronomy, The Johns Hopkins University, 366 Bloomberg Center, 3400 N. Charles Street, Baltimore, MD 21218, USA*
[8]*Department of Physics, University of Texas at Arlington, Box 19059, Arlington, TX 76019, USA*
[9]*U.S. Naval Observatory, 3450 Massachusetts Ave NW, Washington, DC 20392-5420, USA*
[10]*Department of Astrophysical Sciences, Princeton University, Princeton, NJ 08544, USA*
[11]*Department of Physics and Astronomy, University College London (UCL), Gower Street, London WC1E 6BT, UK*
[12]*DRF/IRFU/DAp, CEA-Saclay, F-91191 Gif-sur-Yvette, France*
[13]*NRS/AIM, Université Paris Diderot, F-9119, Gif-sur-Yvette, France*
[14]*Department of Physics and Astronomy, Louisiana State University, Baton Rouge, LA 70803, USA*
[15]*Department of Astronomy, University of Virginia, 530 McCormick Road, Charlottesville, VA 22904, USA*
[16]*Osservatorio Astronomico di Trieste, Via Tiepolo 11, Trieste, Italy*
[17]*SOFIA-USRA, NASA Ames Research Center, Mail Stop 232-12, Moffett Field, CA 94035, USA*
[18]*Sterrenkundig Observatorium, University of Ghent, Krijgslaan 281 - S9, B-9000 Ghent, Belgium*
[19]*European Space Research and Technology Centre, Keplerlaan 1, NL-2200 AG, Noordwijk, The Netherlands*
[20]*DARK, Niels Bohr Institute, University of Copenhagen, Jagtvej 128, Copenhagen DK-2200, Denmark*
[21]*Minnesota Institute for Astrophysics, University of Minnesota, 116 Church Street S. E., Minneapolis, MN 55455, USA*
[22]*National Radio Astronomy Observatory, 520 Edgemont Road, Charlottesville, 22903, VA, USA*

[23]*Finnish Centre for Astronomy with ESO (FINCA), University of Turku, FI-20014 Turku, Finland*
[24]*Tuorla Observatory, Department of Physics and Astronomy, University of Turku, FI-20014 Turku, Finland*
[25]*TMT International Observatory, 100 West Walnut Street, Pasadena, CA 91124, USA*
[26]*Departamento de Astronomía y Astrofísica, Universidad de València, C/Dr Moliner 50, E-46100 Burjassot, Spain*
[27]*Observatori Astronòmic, Universitat de València, C. Catedrático Josè Beltrán 2, E-46980 Paterna, València, Spain*
[28]*Jet Propulsion Laboratory, California Institute of Technology, 4800 Oak Grove Dr, Pasadena, CA 91109, USA*
[29]*Department of Physics and Astronomy, Purdue University, 525 Northwestern Avenue, West Lafayette, IN 47907, USA*
[30]*Integrative Data Science Initiative, Purdue University, WestLafayette, IN 47907, USA*
[31]*Istituto Nazionale di Astrofisica-Osservatorio Astronomico di Palermo, Piazza del Parlamento 1, I-90134 Palermo, Italy*
[32]*Department of Science, Kyoto University, Asakuchi-shi, Okayama Observatory, Okayama, 719-0232, Japan*
[33]*JBCA, School of Physics and Astronomy, University of Manchester, Manchester M13 9PL, UK*
[34]*International Centre for Radio Astronomy Research (ICRAR), The University of Western Australia, 35 Stirling Hwy, Crawley, WA 6009, Australia*
[35]*Steward Observatory, University of Arizona, 933 N. Cherry Ave., Tucson, AZ 85721, USA*
[36]*ESO, Karl-Schwarzschild-Str 2, Garching D-85748, Germany*
[37]*Anton Pannekoek Institute for Astronomy, University of Amsterdam, Science Park 904, NL-1098 XH Amsterdam, the Netherlands*
[38]*GRAPPA, University of Amsterdam, Science Park 904, NL-1098 XH Amsterdam, the Netherlands*
[39]*SRON, Netherlands Institute for Space Research, Sorbonnelaan 2, NL-3584 CA, Utrecht, the Netherlands*
[40]*Department of Physics and Astronomy, Texas A&M University, College Station, TX 77843, USA*
[41]*Cosmic Dawn Center (DAWN), Københavns Universitet, Rådmandsgade 62, DK-2200 København, Denmark*
[42]*Niels Bohr Institute, University of Copenhagen, Jagtvej 128, Copenhagen DK-2200, Denmark*
[43]*Department of Astronomy, The University of Texas at Austin, 2515 Speedway, Austin, TX 78712-1205, USA*
[44]*Department of Astronomy and Astrophysics, Penn State University, University Park, PA 16802, USA*

This paper has been typeset from a TEX/LATEX file prepared by the author.